

# High – Speed Compressible Flow over Blunt and Re-entry Bodies and Validation of Experimental Results

Ishar Singh Saini<sup>1</sup>

<sup>1</sup>Department of Aerospace Engineering, Amity University Mumbai, Panvel, Maharashtra

Biraj Khadka<sup>2</sup>

<sup>2</sup>Research Associate, FOSSEE, IIT Bombay, Maharashtra

Dr. Tushar Chourushi<sup>1,\*</sup>

<sup>1,\*</sup>Department of Aerospace Engineering, MIT-ADT University, Pune, Maharashtra

## ABSTRACT

This project aims to simulate the supersonic/hypersonic flow over some blunt bodies using the sonicFoam solver which is part of the open-source software OpenFOAM and verify the obtained aerodynamic forces with the available results. The use of a blunt shape considerably reduces aero heating over the missiles and blunt shaped bodies but leads to increased drag which is quite useful when during a re-entry from space. The experimental results for bow-shocks of Kim, Chul-Soo [1] for a cylindrical body were validated in this study. Post validation, re-entry geometries which were taken from cases run by R.C. Mehta [2] [4] [5] are introduced in the flow and the aerodynamic parameters were calculated. Standard atmospheric values are used for air at sea level and varying the Mach numbers.

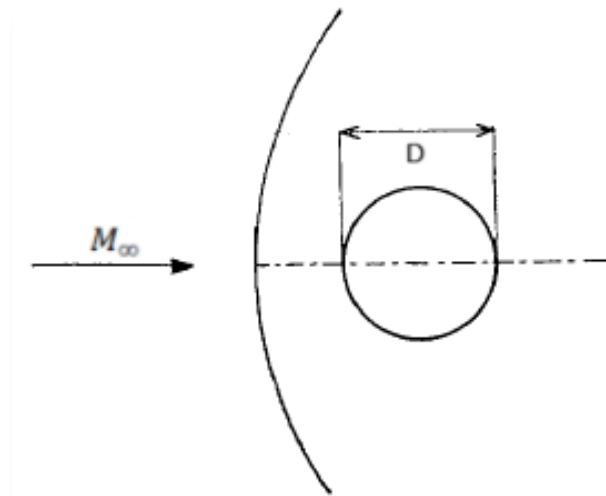


**Figure 1. A Brief of Flow Domain over the Cylindrical body**  
**Figure taken and edited from “Experimental Studies of Supersonic**  
**Flow past a Circular Cylinder”, Kim, Chul-Soo [1]**

# Contents

1. Introduction	(1)
2. Aerodynamic Effects	(3)
2.1 Shock waves and Expansion fans	(3)
2.2 Aerodynamic Parameters	(4)
3. Theory	(5)
3.1 Primary Solver and Governing Equations	(5)
3.2 Turbulence Modelling	(5)
4. Validation – 2D Cylinder	(7)
4.1 Geometry	(7)
4.2 Solver Setup and Boundary Conditions	(7)
4.3 Meshing	(9)
4.4 Grid Independence Study	(9)
4.5 Results – Validation	(11)
4.5.1 Convergence Analysis	(11)
4.5.2 $d/D$ vs Mach number	(12)
4.5.3 $1/b$ vs Mach number	(12)
4.5.4 Pressure Distribution	(13)
4.5.5 Schlieren Graphs and Shock stand-off	(15)
4.5.6 Isopycnics and Streamlines	(16)
4.5.7 Velocity over the body	(16)
4.5.8 Temperature contours	(17)
4.5.9 Aerodynamic Drag	(17)
5. Post Validation – Re-entry Bodies	(19)
5.1 Geometry	(19)
5.2 Solver Setup and Boundary Conditions	(20)
5.3 Meshing	(20)
5.4 Results	(23)
5.4.1 Schlieren Graphs and Shock distances	(23)
5.4.2 Velocity over the body	(25)
5.4.3 Pressure Distribution	(27)

5.4.4 Temperature Contours	(29)
5.4.5 Drag Estimation	(31)
6. Conclusion	(32)

## List of Figures

1. A Brief of Flow Domain over the Cylindrical body	
1.1 Visualization of shock wave over a circular cylinder in a shock tube	(1)
3.1 Shock Waves across different concept bodies	(2)
3.2 Shock Waves and Expansion Fans across different concept bodies	(4)
3.3 Geometry for 2D cylinder	(7)
3.4 Boundary Conditions Schematic	(8)
3.5 Mesh for the Cylinder Case	(6)
3.6 Grid Independence Plot comparing $C_D$ vs number of cells.	(8)
4.1 sonicFoam's Residual Plots	(9)
4.2 $d/D$ vs $M_1$	(10)
4.3 $1/b$ vs $M_1$	(11)
4.4 $C_p$ vs $\theta^\circ$	(13)
4.5 Schlieren Graphs with shock stand-off distances	(14)
4.6 Isopycnics and streamlines	(15)
4.0 Mach number contours	(19)
4.0 Temperature contours	(19)
4.0 Geometric Representation of Re-entry bodies	(19)
4.0 Reference Meshes of Re-entry capsules	(19)
4.0 Mesh for the Apollo Capsule	(19)
4.0 Mesh for the ARD Capsule	(19)
4.0 Mesh for the OREX Capsule	(19)
4.0 Schlieren Graph for Apollo	(19)
4.0 Schlieren Graph for ARD	(19)
4.0 Schlieren Graph for OREX	(19)
4.0 Mach contours for Apollo	(19)
4.0 Mach contours for ARD	(19)

4.0 Mach contours for OREX	(19)
4.0 Pressure Distribution for the Apollo Capsule	(19)
4.0 Pressure Distribution for the ARD Capsule	(19)
4.0 Pressure Distribution for the OREX Capsule	(19)
4.0 Temperature Contours for Apollo	(19)
4.0 Temperature Contours for ARD	(19)
4.0 Temperature Contours for OREX	(19)

## **List of Tables**

1. Relaxation Factors	(5)
2. Flow Parameters for cylindrical body case	(7)
3. Boundary Conditions	(8)
4. Boundary Conditions (Turbulence Model)	(8)
5. Mesh Quality Table	(9)
6. Drag Coefficient Variation in Grid Independence	(10)
7. Shock stand-off values	(15)
8. Final Aerodynamic Results	(18)
9. Geometrical parameters of re-entry capsules	(19)
10. k- $\epsilon$ model values for the cylinder	(20)
11. Mesh Quality Table (Apollo)	(21)
12. Mesh Quality Table (ARD)	(22)
13. Mesh Quality Table (OREX)	(22)
14. Shock distances for all bodies	(25)
15. Drag values for all bodies	(31)

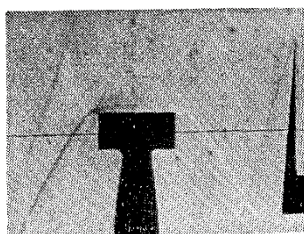
# Chapter 1

## Introduction

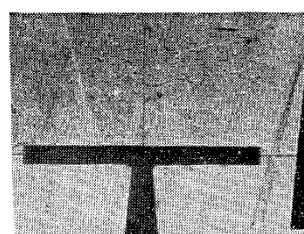
Re-entry bodies, such as space capsules and hypersonic vehicles, experience extreme thermal and aerodynamic loads as they re-enter a planetary atmosphere. Understanding the complex flow phenomena, including shock wave interactions, boundary layer behavior, and aerodynamic heating, is crucial for the design and safety of these vehicles. CFD provides a powerful tool for simulating these high-speed flows and predicting the aerodynamic performance of re-entry bodies. However, the accuracy of CFD predictions must be rigorously validated against experimental data to ensure their reliability.

Our study focuses to validate a supersonic flow over an 2D cylinder (Diameter – 1m) with fluid properties as of sea level air and to simulate the same flow over re-entry bodies.

Kim, Chul-Soo [1] conducted experimental studies in a shock tube to determine the shape of detached shocks from a circular cylinder and to compare with theoretical calculations over a range of Mach numbers. Their results showcased an important key point: Two dimensionality is obtained at aspect ratio ( $L/D$ ) which is greater than 5.5 for Mach number range of 2.7 to 6.0. In this study we try to validate the validate these results and the comparison of shock structure in this Mach number range. Figure 1.1 shows the visualization of two dimensionality caused as the  $L/D$  is increased.



A)  $L/D = 2.0$  (Pg: 441, [1])



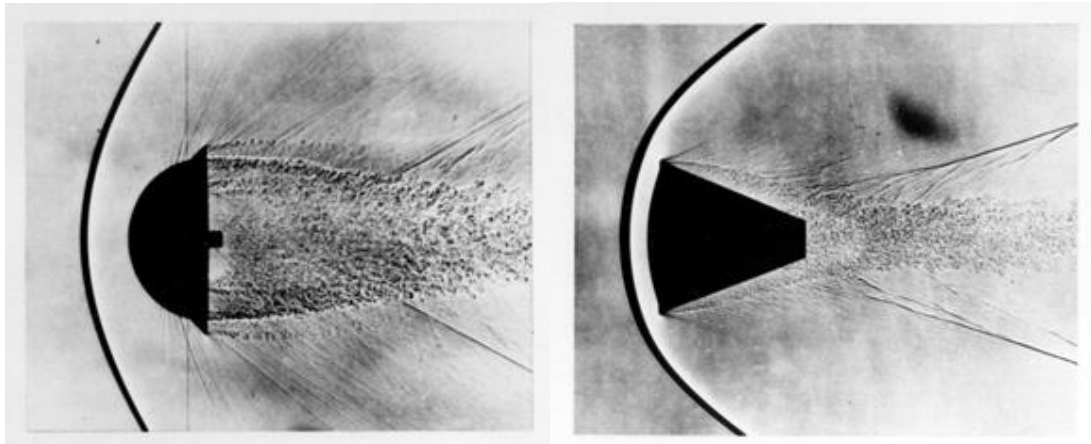
B)  $L/D = 13.4$  (Pg: 441, [1])

Figure 1.1 Visualisation of shock wave over a circular cylinder in a shock tube, “*Experimental Studies of Supersonic Flow past a Circular Cylinder*”, Kim, Chul-Soo [1]

The Numerical study of R.C. Mehta [2] [4] [5] shows the heat transfer and aerodynamic forces over various re-entry configurations by solving time-dependent compressible laminar Navier-Stokes equations and the results showcase comparisons of the flow field, surface pressure distribution and wall heat flux results are made between different configurations of the re-entry capsules with freestream Mach number 5 and standard air conditions at 29 km altitude. We implement the re-entry capsules of Apollo, ARD (ESA’s Atmospheric Re-entry Demonstrator) and OREX (Orbital Re-entry Experiments).

The effect of aerodynamic drag and aerodynamic heating has always been a major issue in the hypersonic regime. To get the desired effects of how the body should behave in such flow, we optimize the body to be blunt to have higher drag, but this also increases the heating with the cube of velocity. Thus, the bodies need to be considered to have an insulated layer on them to further assume in the numerical study for an isothermal wall.

Cylindrical and high drag optimized bodies have been a concept to slow down high Mach re-entries to a speed where the body can land safely on the surface. Such concepts are shown below in Figure 1.2.



A. Blunt Body Concept 1953

B. Re-entry Manned Capsule Concept 1957

Figure 1.2 Shock Waves across different concept bodies [12]

## Chapter 2

# Aerodynamic Effects

### 2.1 Shock waves and Expansion Fans

In the field of high-speed aerodynamics, the study of shock waves and expansion fans is crucial for understanding the flow behavior around blunt bodies, such as space capsules and hypersonic vehicles. These phenomena are especially significant during atmospheric re-entry, where vehicles encounter extreme aerodynamic conditions that influence their stability, thermal protection, and structural integrity.

Shock waves are abrupt, nearly discontinuous changes in pressure, temperature, and density that occur when a supersonic flow encounters an obstacle or when two supersonic flows interact. They are characterized by a sudden increase in pressure and temperature, which results in significant aerodynamic heating. When a blunt body travels at hypersonic speeds through an atmosphere, a strong bow shock wave forms ahead of the body. This bow shock is detached from the surface, creating a highly complex flow field between the shock and the body surface. The interaction of the bow shock with the boundary layer on the body's surface leads to various flow phenomena, such as shock-boundary layer interactions, which can result in increased aerodynamic drag and localized heating. Understanding the characteristics of these shock waves, including their position, strength, and structure, is essential for designing effective thermal protection systems and ensuring the aerodynamic performance of re-entry vehicles.

In contrast to shock waves, expansion fans are regions where the flow undergoes a gradual and continuous expansion. These fans occur when a supersonic flow turns away from itself, causing a decrease in pressure and temperature. Expansion fans are composed of a series of infinitesimal expansion waves that spread out from a sharp corner or convex surface. For blunt bodies, expansion fans are typically observed in areas where the surface geometry changes, such as at the trailing edges or around control surfaces. These fans contribute to the overall flow field by reducing the pressure and temperature gradients, thus affecting the aerodynamic forces and moments acting on the vehicle. Properly accounting for expansion fans in aerodynamic analyses is critical for accurately predicting the performance and stability of re-entry bodies.



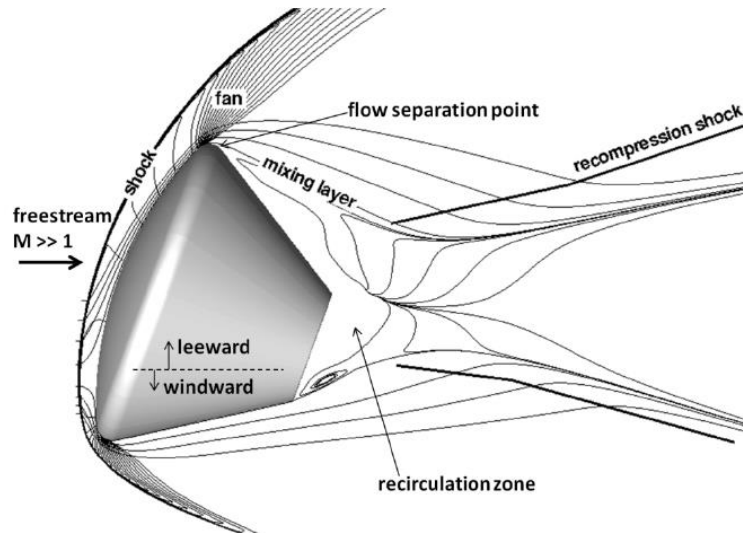


Figure 2.1 Shock Waves and Expansion Fans across different concept bodies [13]

## 2.2 Aerodynamic Parameters

Understanding and managing aerodynamic forces is a fundamental challenge in the design and operation of flight vehicles. Pressure distribution is a critical aspect of aerodynamics, especially in the context of re-entry bodies and high-speed flows. It refers to the variation of pressure over the surface of an object as it interacts with the surrounding fluid flow. Understanding pressure distribution is essential for predicting aerodynamic forces such as lift and drag, as well as for assessing structural loads and thermal stresses on the vehicle. Drag is the aerodynamic force that opposes the motion of an object through a fluid, such as air, and it plays a crucial role in determining an object's speed, efficiency, and fuel consumption.

Here, we compare our aerodynamic results in terms of **drag coefficient and pressure coefficient**.

$$C_D = \frac{2D}{\rho_{\infty} V_{\infty}^2 A} \qquad C_P = \frac{p - p_{\infty}}{\frac{1}{2} \rho_{\infty} V_{\infty}^2}$$

where  $C_D$  = Drag Coefficient

$C_P$  = Pressure Coefficient

$D$  = Drag Force

$p$  = Local Pressure

$p_{\infty}$  = Free-stream Pressure

$\rho_{\infty}$  = Free-stream Density

$V_{\infty}$  = Free-stream Velocity

$A$  = Reference Area

(Note: The density is taken as 1.17662 kg/m<sup>3</sup> for all the cases and the reference area is the area of the circle (2D cylinder) which is 0.7854 m<sup>2</sup>.)

## Chapter 3

### Theory

#### 3.1 Primary Solver and Governing Equations

SonicFoam is a Transient pressure-based solver for trans-sonic/supersonic, turbulent flow of a compressible gas that uses PIMPLE algorithm in this case to solve the equations. The PIMPLE Algorithm is a combination of PISO (Pressure Implicit with Splitting of Operator) and SIMPLE (Semi-Implicit Method for Pressure-Linked Equations). The flow regime in this case is mainly governed by compressible Navier-Stokes equations;

- Mass Continuity

$$\frac{\partial \rho}{\partial t} + \nabla \cdot (\rho \mathbf{U}) = 0 \quad (3.1)$$

- Momentum Continuity for Newtonian Fluid

$$\frac{\partial \rho \mathbf{U}}{\partial t} + \nabla \cdot [\mathbf{U}(\rho \mathbf{U})] - \nabla \cdot \mu \nabla \mathbf{U} = -\nabla p - \nabla \sigma \quad (3.2)$$

- Energy Equation for fluids,  $e = C_v T$ , with Fourie's Law  $q = -k \nabla T$

$$\frac{\partial \rho e}{\partial t} + \nabla \cdot (\rho \mathbf{U} e) - \nabla \cdot \left( \frac{k}{C_v} \right) \nabla e = p \nabla \cdot \mathbf{U} \quad (3.3)$$

- Ideal Gas Law

$$p = \rho R T \quad (3.4)$$

SonicFoam solver is typically used to solve high Mach number cases which involves analysis of shock wave formations and aerodynamic drag on bodies.

In the solution algorithm, we also incorporate the use of relaxation factors with the following values:

Relaxation Factors	Parameters	Values
Fields	U	0.6
	p	0.4
Equations involving the parameters	U	0.7
	k	0.7
	$\epsilon$	0.7

Table 1: Relaxation Factors

#### 3.2 Turbulence Modeling

Reynold's number typically describes the turbulence in the flow.

$$\text{Re} = \frac{\rho v L}{\mu} = \frac{v L}{\nu}$$

where  $v$  being the characteristic velocity which in this case is the freestream velocity  $u_\infty$ , and  $\nu$  being the kinematic viscosity. The characteristic length ( $L$ ) here is defined as the length of a side of the prism.

Standard K-epsilon turbulence model was used in this case. It is a Two transport equation linear-eddy-viscosity turbulence closure model where the two transport variables are turbulent kinetic energy,  $k$  and turbulent kinetic energy dissipation rate,  $\epsilon$ .

The **turbulent kinetic energy** equation,  $k$ :

$$\frac{D}{Dt}(\rho k) = \nabla \cdot (\rho D_k \nabla k) + P - \rho \epsilon$$

The **turbulent kinetic energy dissipation** rate equation,  $\epsilon$ :

$$\frac{D}{Dt}(\rho \epsilon) = \nabla \cdot (\rho D_\epsilon \nabla \epsilon) + \frac{C_1 \epsilon}{k} (P + C_3 \frac{2}{3} k \nabla \cdot u) - C_2 \rho \frac{\epsilon^2}{k}$$

The **turbulent viscosity** equation,  $\nu_t$

$$\nu_t = C_\mu \frac{k^2}{\epsilon}$$

Standard K-epsilon turbulence model was used in this case. It is a Two transport equation linear-eddy-viscosity turbulence closure model where the two transport are  $k$  and  $\epsilon$ .

Further, from the work of Versteeg [17], the values for a few specific constants like  $C_\mu$ ,  $C_1$ ,  $C_2$ , have been set. For calculating turbulent intensity ( $I$ ), the formula for a fully developed pipe flow is used.

$$I = 0.16 \times Re^{(-\frac{1}{8})}$$

For our case,  $I$  will be around  $0.034 \sim 3\%$ . This is used to calculate various  $k$  and  $\epsilon$  values for various velocities.

For isotropic turbulence, the turbulent kinetic energy can be estimated by:

$$k = \frac{3}{2} (I |\mathbf{u}_{ref}|)^2$$

where,  $u_{ref}$  is reference flow speed.

For isotropic turbulence, the turbulence dissipation rate can be estimated by:

$$\epsilon = \frac{C_\mu^{0.75} k^{1.5}}{L}$$

where,  $C_\mu$  is model constant equal to 0.09 by default.

$L$  is reference length (m)

## Chapter 4

### Validation – 2D Cylinder

#### 4.1 Geometry

For the validation of Kim's [1] experimental results, we construct a domain similar to that of the experiment. Here, we have went for circular domain 10 times the diameter to visualize the flow. Here, the diameter is taken as unity as the flow doesn't depend on the size, but entirely on the shape.

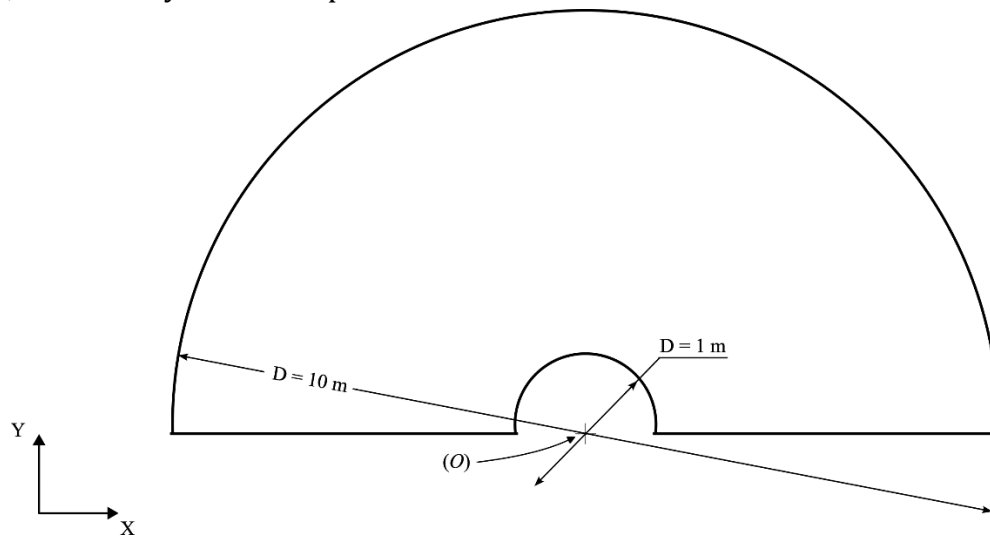


Figure 4.1 Geometry for 2D cylinder

#### 4.2 Solver Setup and Boundary Conditions

As per the experiment [1], the flow speed for higher  $L/D$  were set for Mach 2.7, 4 and 6. Standard sea-level air conditions are modelled for the simulations with the following parameters given below.

Mach number	Inlet velocity (u)	Pressure (p)	Temperature (T)	Viscosity ( $\mu$ )	Density ( $\rho$ )
2.7	926.1 m/s	101325 Pascals	300 K	$1.5689 \times 10^{-5} \text{ N.s.m}^{-2}$	$1.17662 \text{ kg/m}^3$
4	1372 m/s				
6	2058 m/s				

Table 2: Flow Parameters for cylindrical body case

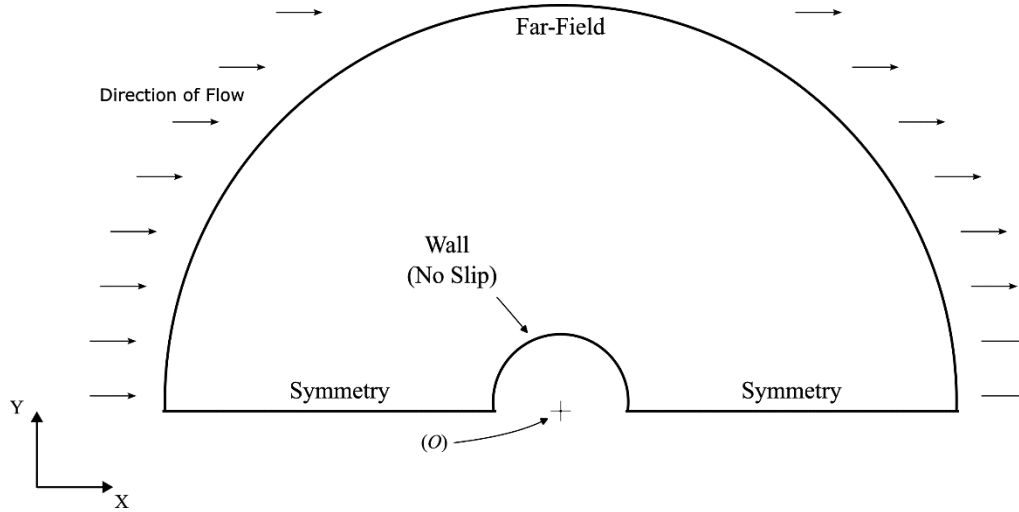


Figure 4.2: Boundary Conditions Schematic (All the domain boundaries have been named far - field as they have the same patch type but different patch names)

The following table shows the different patch types used for different patches for the initial conditions.

Variable	FARFIELD	Symmetry	Wall
Pressure (p)	zeroGradient	symmetry	zeroGradient
Temperature (T)	inletOutlet	symmetry	zeroGradient
Velocity (u)	supersonicFresstream	symmetry	noSlip

Table 3: Boundary Conditions

For the turbulence model, k -  $\epsilon$  model values are given below.

Mach number	Reynold's Number	Turbulence Intensity (I)	Turbulent Kinetic Energy (k)	Rate of dissipation of k ( $\epsilon$ )
Mach 2.7	$6.945 \times 10^7$	0.0167	358.7897	1116.7137
Mach 4	$1.029 \times 10^8$	0.0159	713.8282	3133.8084
Mach 6	$1.543 \times 10^8$	0.0152	1467.8077	9240.2905

Table 4: Boundary Conditions

## 4.3 Meshing

Structured meshes were produced in ICEM CFD.

### 4.3.1 Mesh

The 2D grid for the cylinder case has 60k hexahedral cells which is made finer around the body with inflation layers.

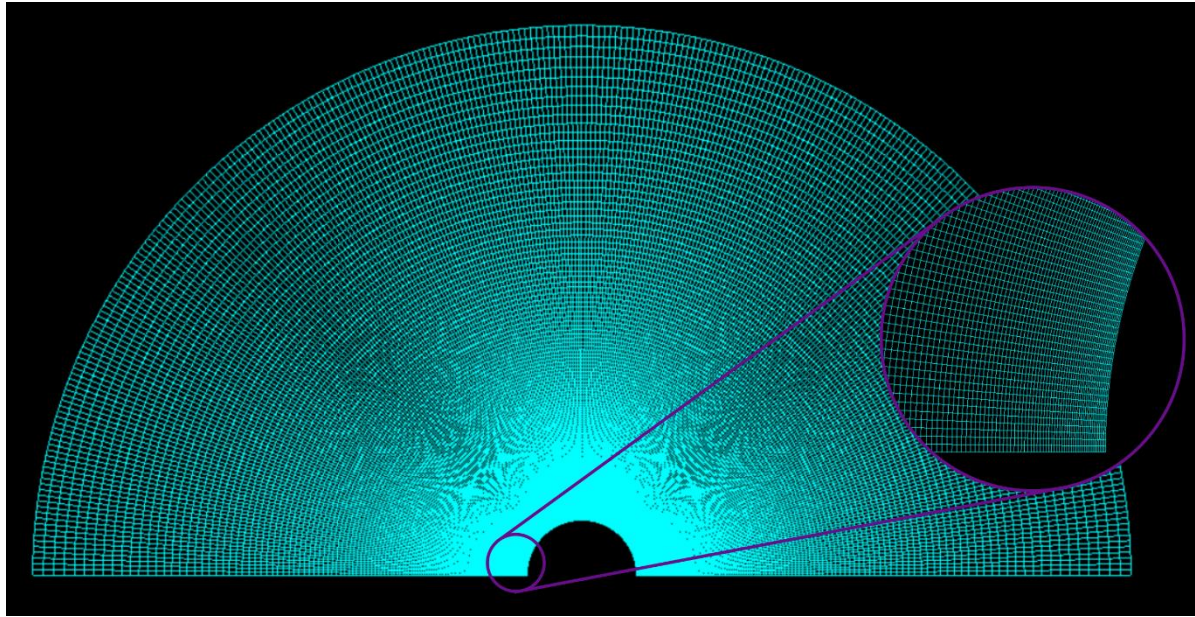


Figure 4.3 Mesh for the Cylinder Case

### 4.3.2 Mesh Quality

The mesh quality report has been generated by the 'checkMesh' command in openFoam.

Mesh Parameter	Value
Max aspect ratio	3.94059
Max non-orthogonality	$4.82967 \times 10^{-06}$ Average: 0
Max skewness	0.0128199
Max cell openness	$2.5044 \times 10^{-16}$

Table 5: Mesh Quality Table

## 4.4 Grid Independence Study

A grid independence study has been conducted Mach number 2.7. A grid independence study is a CFD solution that doesn't rely on the type of mesh or the size of mesh that is being used, i.e., it removes the subjectivity of the solution and makes it more general. In the current study, the size biasing is varied and the minimum size at which a general solution is obtained is used as a reference or baseline upon which mesh independence can be proved.

As we progress to make new meshes, the mesh sizing is made to be finer and finer around the body to capture the full effect of the boundary layers with the increase of mesh elements. The mesh size is reduced progressively coarse size to a fine mesh size and the variation in flow parameters is checked. When the percentage difference between the two successive meshes is negligible, the coarser mesh is finalised to be used for the rest of the simulations. Mesh independence forms an important part of CFD study to ensure that least computational resources are utilized.

For this study, five meshes were used and the size is reduced by the technique used by experts i.e., by doubling the mesh element count of the preceding coarser mesh. The table 5. shows the variation of the drag coefficient for the different meshes for the cylindrical domain.

Mesh Size	Drag	Result Variation %
15k	0.146	-
30k	0.179	-0.925
60k	0.194	-0.714
120k	0.197	-0.139
240k	0.1968	

Table 6: Drag Coefficient Variation in Grid Independence

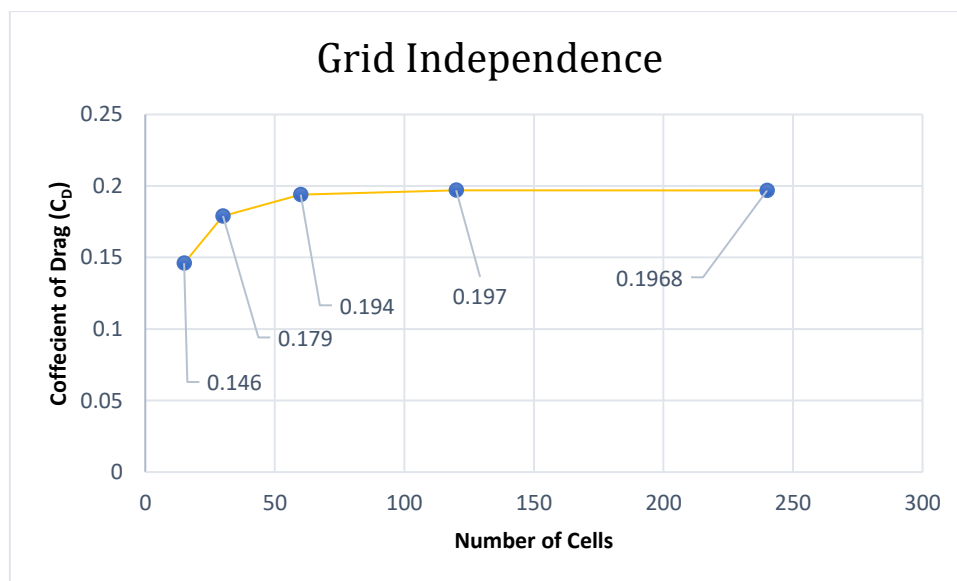


Figure 4.4: Grid Independence Plot comparing  $C_D$  vs number of cells.

As the error of drag force is quite less between the 60k and 120k mesh, the medium sized mesh of 60k cells has been chosen for the further study.

## 4.5 Results – Validation

The experimental results are validated by comparing 3 plots in the reference. [1]

### 4.5.1 Convergence Analysis

The residuals are one of the most fundamental measures of an iterative solution's convergence, as it directly quantifies the error in the solution of the system of equations. In a CFD analysis, the residual measures the local imbalance of a conserved variable in each control volume. Therefore, every cell in the model will have its own residual value for each of the equations being solved. Figure 4.1 shows the residuals of sonicFoam simulation at Mach number 2.7 representing that the simulation has attained a steady-state on time  $t = 0.02s$  plotted using pyFoam.

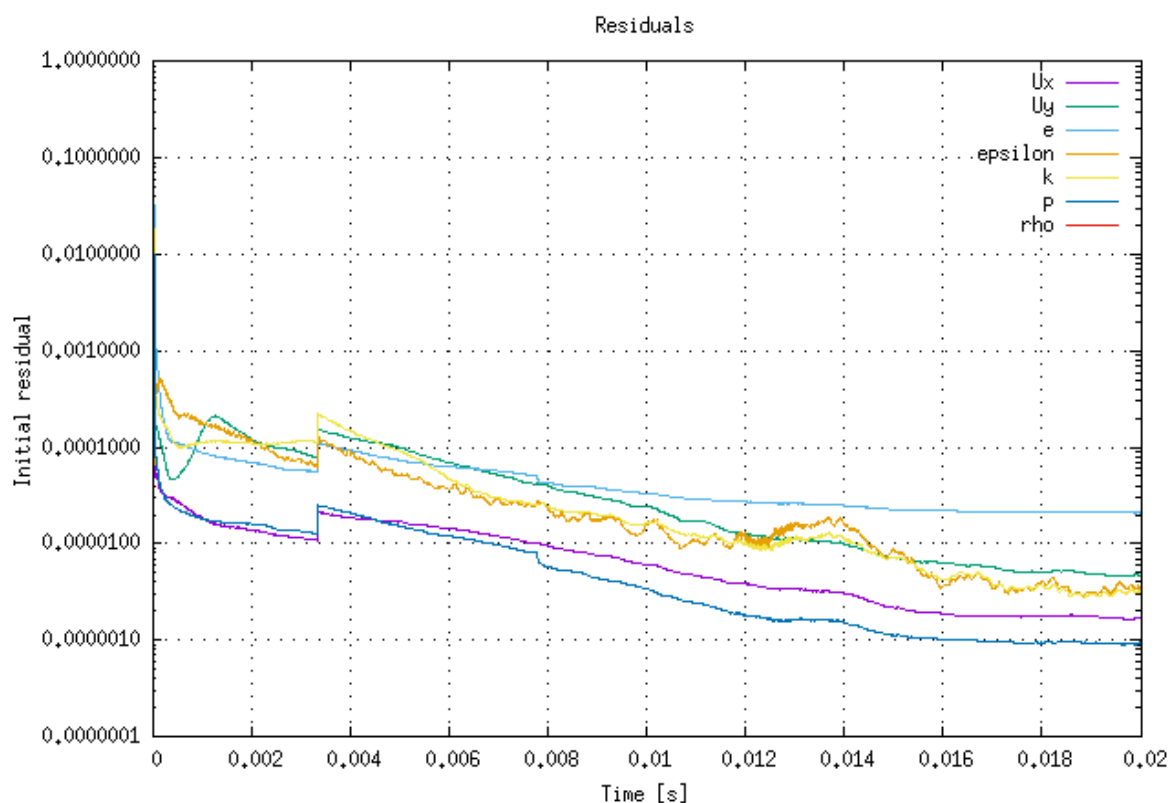


Figure 4.5 : simpleFoam's Residual Plots



### 4.5.2 $d/D$ vs Mach number

$d/D$  ratio is the ratio of shock stand-off distance ( $d$ ) to the diameter of the cylinder ( $D$ ). This plot describes the shock structure with the increase in Mach no. We refer Fig 4.6 for the  $d/D$  values of the present experiment marked by white circle ( $\bigcirc$ ) and Fig 4.7 shows the comparison of sonicFoam's results and the reference experimental results. In fig, we have highlighted the required values with a red circle.

The sonicFoam's results matches well with the experiments at a lower Mach number. However, as the Mach number increases, the shock wave comes out to be much closer to the body in the simulation as compared to the experiment. Thus, at Mach 6, the sonicFoam values seems much lower.

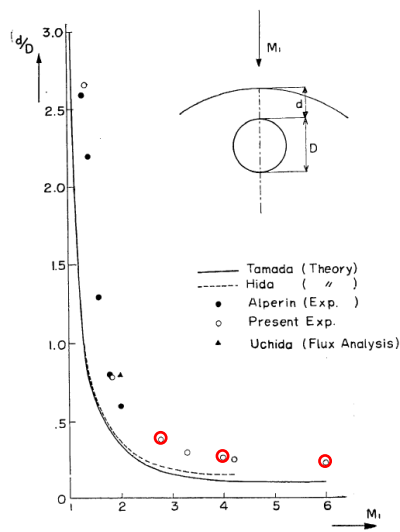


Figure 4.6: Kim, Chul-Soo's [1]  $d/D$  vs  $M_1$

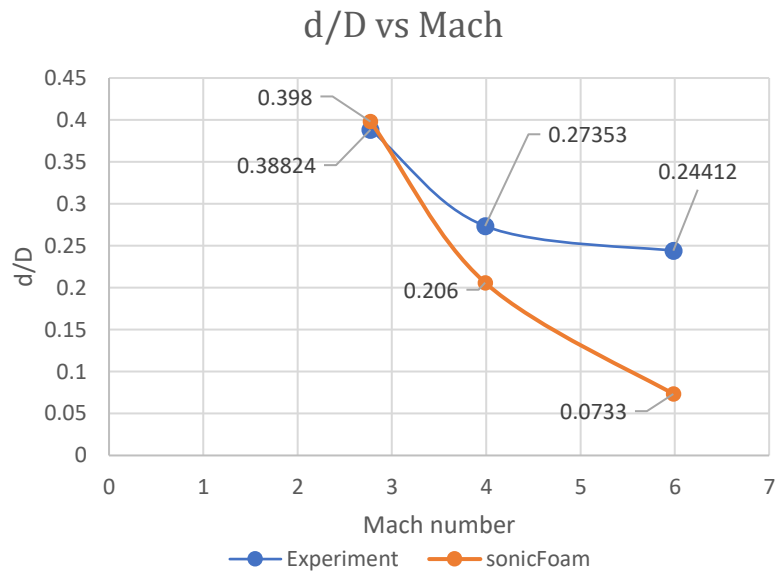


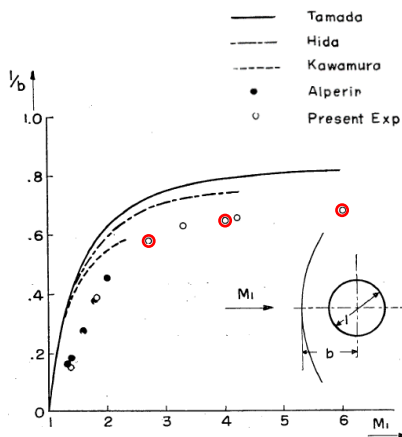
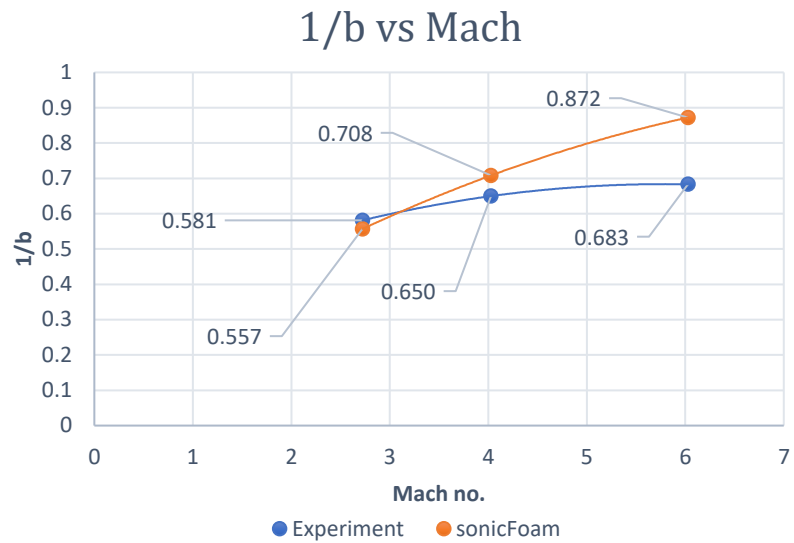
Figure 4.7 : Validation plot for  $d/D$  vs  $M_1$

### 4.5.3 $1/b$ vs Mach number

Fig 4.8 shows the relation between the inverse of ' $b$ ' and  $M_1$  where ' $b$ ' can be expressed as, [1]

$$b = (D + 2d)/D$$

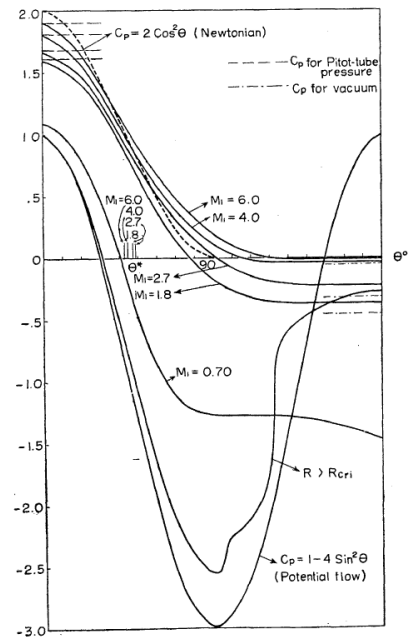
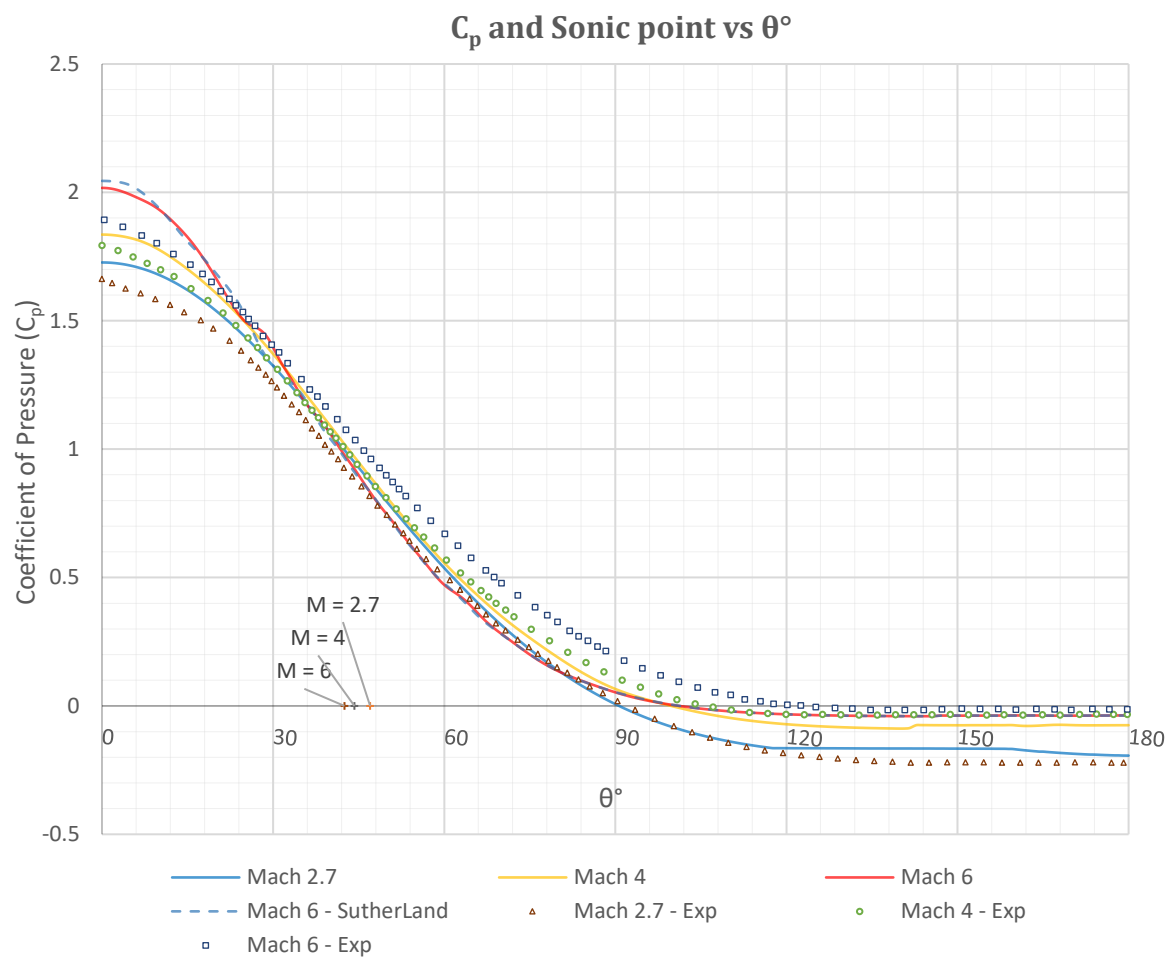
In simple terms, ' $b$ ' can be said to be the distance between the centre of the cylinder to the shock. The present experiment has been marked again by white circles ( $\bigcirc$ ) and we have again highlighted the required values with red circles. Fig 4.9 shows the comparison with sonicFoam's results and we can see similar comparison as of the  $d/D$  vs Mach number plots.

Figure 4.8 : Kim, Chul-Soo's [1]  $1/b$  vs  $M_1$ Figure 4.9 : Validation plot for  $1/b$  vs  $M_1$ 

#### 4.5.4 Pressure Distribution

The pressure distribution over the cylinder in the experiments is shown through the  $C_p$  vs  $\theta^\circ$  plot which compares various theories with other reference experiments. In the Fig 4.10, the pressure coefficients against  $\theta$  are shown in full lines for  $M_1 = 1.8, 2.7, 4.0$  and  $6.0$  [1]. For this validation, we only consider  $M_1 = 2.7, 4.0$  and  $6.0$  for which the comparison is shown in Fig 4.11. Here, we also show the sonic points of the experiment.

From the comparison, we can see that the stagnation pressures for all the velocities are larger than experimental values. Also, the pressure values are lower than the experiment on the rearward side of the cylinder for all the velocities as well. For  $M_1 = 6$ , the pressure drops rapidly after  $\theta = 30^\circ$ , dropping lower than that of the lower Mach numbers, which as per the experiment and the theory can be proven wrong. For this reason, we have also tried to implement Sutherland's transport model for Mach 6. But, from the plot we can tell it doesn't show any major changes in the results. This shows the limitation of sonicFoam for hypersonic flows.

Figure 4.10 : Kim, Chul-Soo's [1]  $C_p$  vs  $\theta^\circ$ Figure 4.11 : Validation for  $C_p$  vs  $\theta^\circ$

#### 4.5.5 Schlieren Graphs and Shock Stand-off

To visualize the shock waves and expansion fans, Schlieren graphs are often used which shows the gradient of density ( $\nabla\rho$ ) of the flowfield. This technique is used to visualize the shocks over the body in supersonic flows. The following graphs show the shock structure along with the shock stand-off distance which is the perpendicular distance between the stagnation point of the body and the shock wave. We can see as expected, the shocks come closer to the body as the velocity increases.

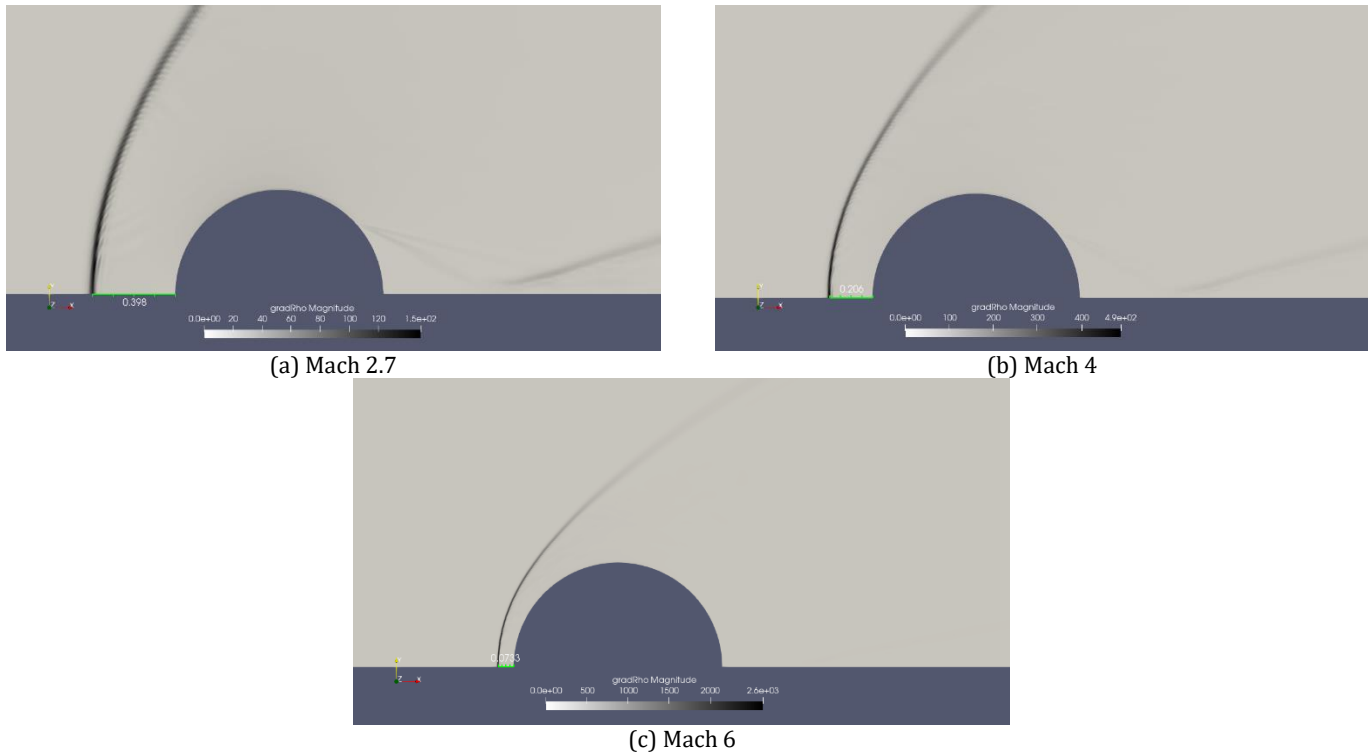


Figure 4.12 : Schlieren Graphs with shock stand-off distances

Mach number	Shock stand-off distance (d)
2.7	0.398 m
4	0.206 m
6	0.0733 m

Table 7: Shock stand-off values

### 4.5.6 Isopycnics and Streamlines

Fig 4.13 shows isopycnics (contours of constant density) for Mach 4. Streamlines as well as sonic line is also shown in the figure below. Also, figure 4.14 shows the validation plot for the same. We can observe that the contour lines are almost running similar to that of the experiment and the deviation of the streamlines are also similar. From this simulation as well as the experiment, we can conclude that the streamlines in the subsonic region behind the shock are nearly straight and parallel to each other except in the vicinity of the cylinder. This suggests that, in sub-sonic region, the vorticity just behind the shock conserves its intensity along each streamline.

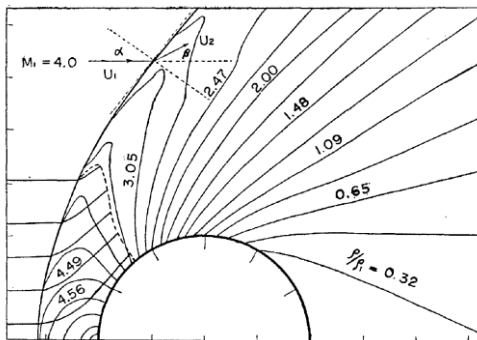


Figure 4.13 : Kim, Chul-Soo's [1] Isopycnics, streamlines and sonic line

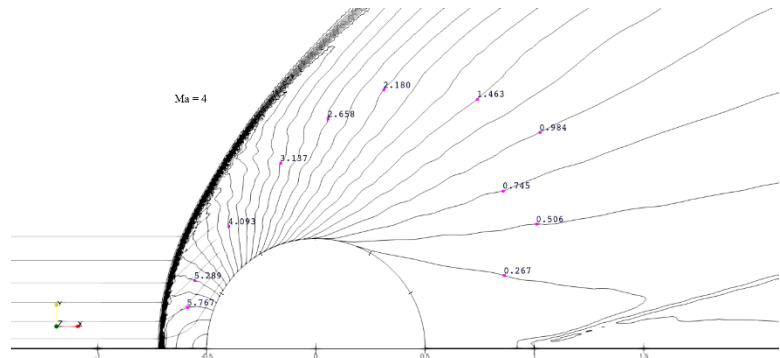
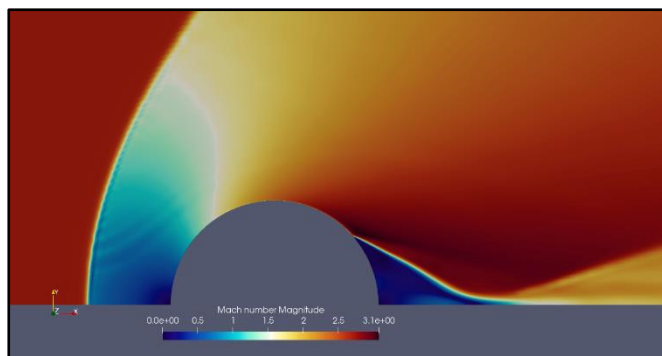


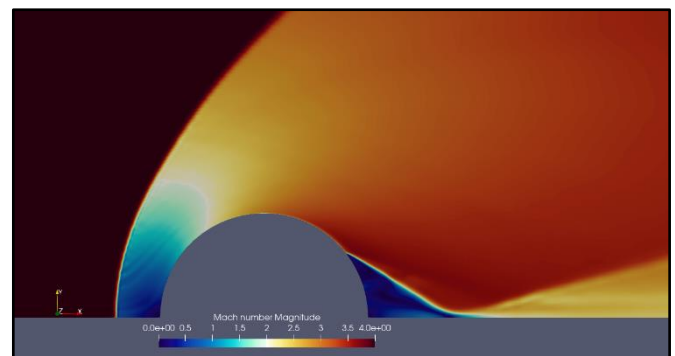
Figure 4.14 : Validation plot for isopycnics and streamlines

### 4.5.7 Velocity over the body

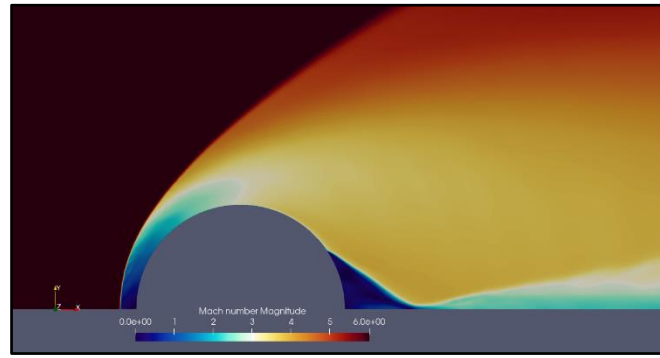
To observe the velocity profile over the cylinder, we use Mach number contours. As expected from the contours, we can see as the velocity increases, the intensity and strength of the shock waves generally increase as well. We can also observe that the increase in velocity also brings the shock closer to the body.



(a) Mach 2.7



(b) Mach 4

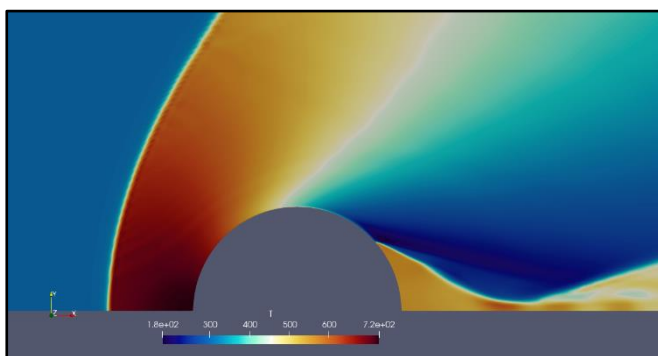


(c) Mach 6

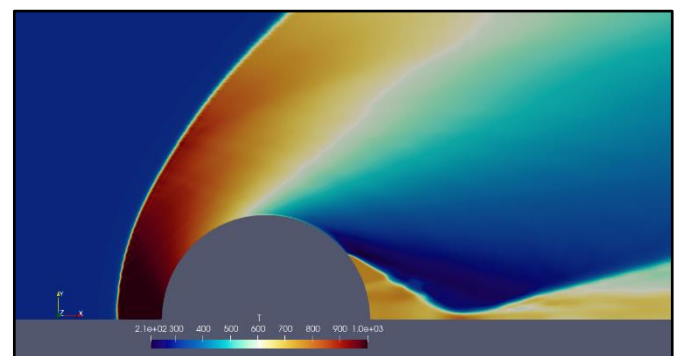
Figure 4.15 : Mach number contours

### 4.5.8 Temperature Contours

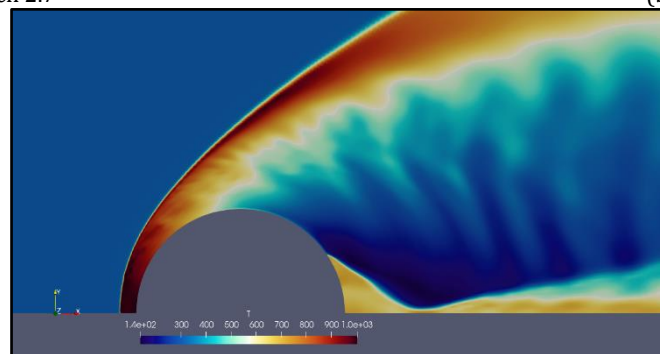
Temperature contours can be used to observe heat dissipation of the blunt body. These can be further used in future work to depict heat transfer due to aerodynamic heating. At  $M_1 = 6$ , we can observe the dissipation more clearly as aerodynamic heating is more dominant at hypersonic speeds.



(a) Mach 2.7



(b) Mach 4



(c) Mach 6

Figure 4.16 Temperature contours

### 4.5.9 Aerodynamic Drag

For re-entry bodies, drag plays a major role to slow down the vehicle when re-entering the atmosphere at hyper-velocity speeds. There were no drag results specified in the experiment [1], however we estimate the results in the simulation as shown in the Table. Drag force is increasing but the  $C_D$  values seem to decrease with the increase in Mach number.

Mach number	Drag Force (N)	Drag Coefficient ( $C_D$ )
2.7	76,635.2	0.193
4.0	1,63,587	0.188
6.0	3,65,468	0.186

Table 8: Final Aerodynamic Results

## Chapter 5

### Post Validation – Re-entry Bodies

After the validation of Kim's experiments [1] we further extend the study by replacing the 2D cylinder shape with some re-entry bodies as used by R.C. Mehta's study in the same flow conditions. [2] [4] [5]

#### 5.1 Geometry

R.C. Mehta's numerical study had made use of 6 different re-entry body shapes but here we only use the first three namely Apollo, ARD and OREX capsules. Fig and table show the geometric details of the three bodies. The domain is similar to that of the validation case as shown earlier in Fig 4.1 i.e. a circular domain but here the far-field is 5 times the maximum diameter of the respective body. Fig 5.1 shows the geometric parameters as per R.C. Mehta's paper. [2] [4] [5]

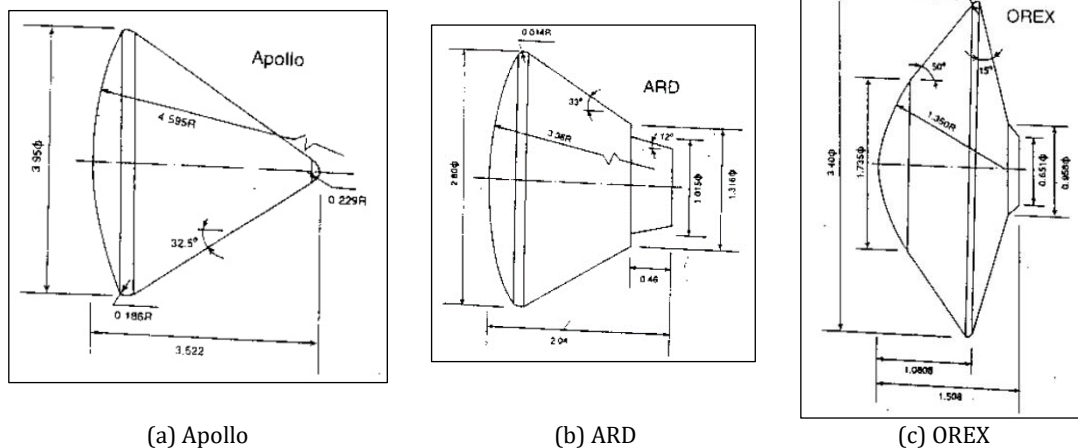


Figure 5.1 Geometric Representation of Re-entry bodies

Capsule	Spherical radius, $R_N$	Frontal diameter, $D$	Corner radius, $R_c$	Overall length, $L$	Semi-cone angle, $\alpha_N$ deg	Back-shell angle, $\alpha_B$ deg
ARD	3.36	2.80	0.014	2.04	-	33.0
Apollo	4.595	3.95	0.186	3.52	-	33.0
OREX	1.35	3.40	0.001	1.50	50	15.0

Figure 9: Geometrical parameters of re-entry capsules



## 5.1 Solver Setup and Boundary Conditions

The boundary conditions and the flow parameters are the same as of the validation case. We can refer to Table 1, fig 3.3 and table 2 for the details of the setup. However, for the turbulence model, the calculated  $k - \epsilon$  model values are given below.

Body	Mach number	Reynold's Number	Turbulence Intensity (I)	Turbulent Kinetic Energy (k)	Rate of dissipation of k ( $\epsilon$ )
Apollo	2.7	$2.446 \times 10^8$	0.0143	263.345	702.214
	4.0	$3.624 \times 10^8$	0.0136	523.894	1970.367
	6.0	$5.436 \times 10^8$	0.0129	1065.131	5711.9766
ARD	2.7	$1.417 \times 10^8$	0.0153	301.866	861.7934
	4.0	$2.099 \times 10^8$	0.0146	600.528	2418.142
	6.0	$3.148 \times 10^8$	0.0139	1220.936	7010.052
OREX	2.7	$1.047 \times 10^8$	0.0159	325.647	965.612
	4.0	$1.552 \times 10^8$	0.0151	600.528	2418.142
	6.0	$2.327 \times 10^8$	0.0144	1316.740	7851.126

Table 10:  $k - \epsilon$  model values for the cylinder

## 5.2 Meshing

Structured meshes were produced in ICEM CFD for all the bodies.

### *Mesh and Grid Quality*

#### A. Reference Meshes

All meshes were produced in reference to R.C. Mehta's meshes. [2] [4] [5]

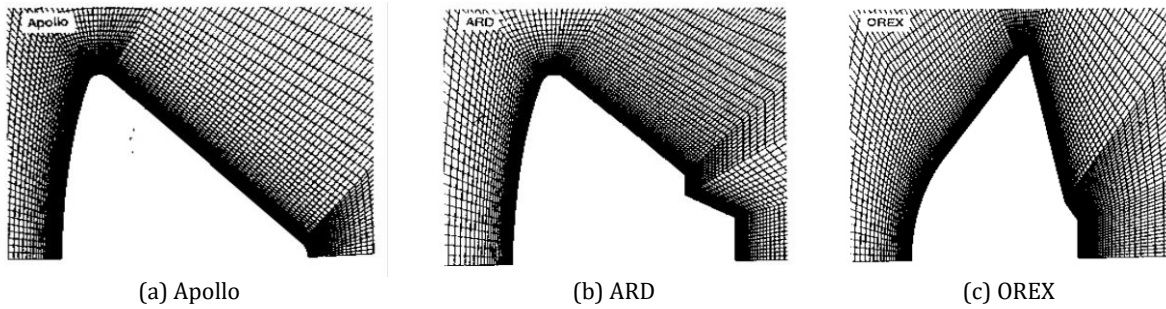


Figure 5.2 Reference Meshes of Re-entry capsules

#### B. Apollo

The 2D grid for the Apollo has 52k hexahedral cells which is made finer around the body with inflation layers.

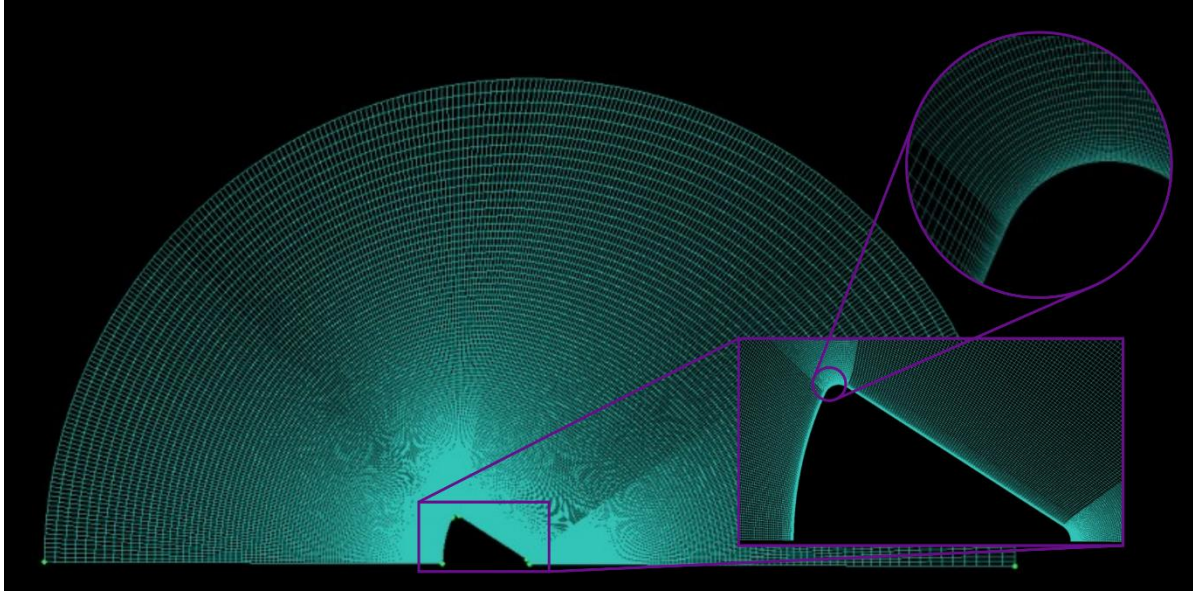


Figure 5.3 Mesh for the Apollo Capsule

The mesh quality report has been generated by the 'checkMesh' command in openFoam.

Mesh Parameter	Value
Max aspect ratio	16.0532
Max non-orthogonality	22.4833 Average: 6.53845
Max skewness	0.423893
Max cell openness	$7.19764 \times 10^{-16}$

Table 11: Mesh Quality Table

### C. ARD

The 2D grid for the ARD has 52k hexahedral cells which is made finer around the body with inflation layers.

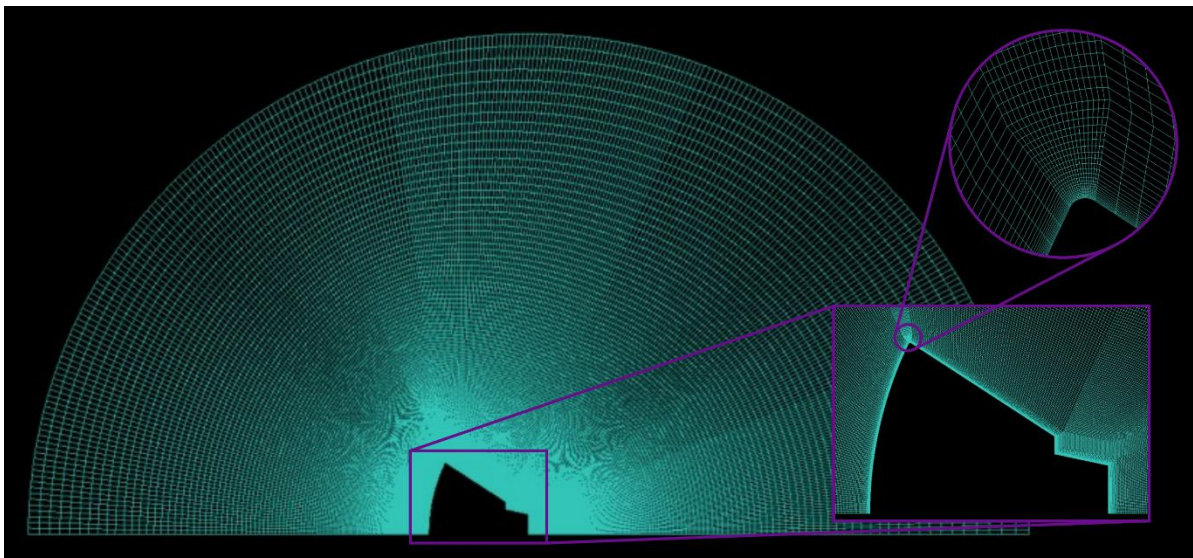


Figure 5.4 Mesh for the Apollo Capsule

The mesh quality report has been generated by the 'checkMesh' command in openFoam.

Mesh Parameter	Value
Max aspect ratio	14.73
Max non-orthogonality	43.1909 Average: 14.232
Max skewness	2.01166
Max cell openness	$8.37954 \times 10^{-16}$

Table 12: Mesh Quality Table

#### D. OREX

The 2D grid for the OREX has 55k hexahedral cells which is made finer around the body with inflation layers.

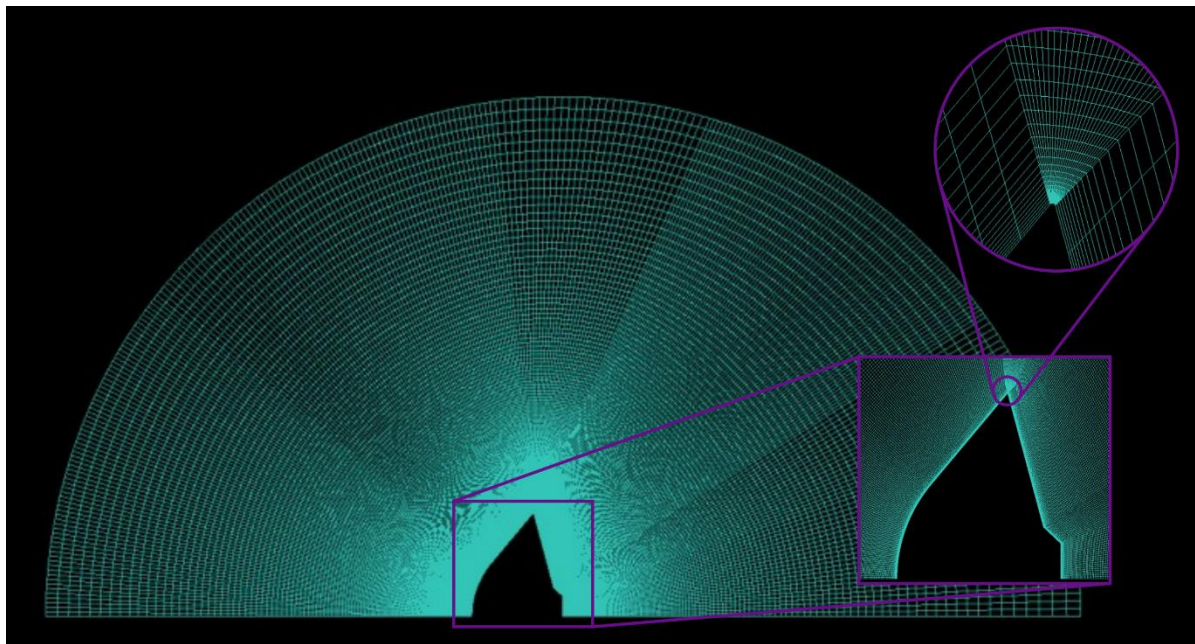


Figure 5.4 Mesh for the Apollo Capsule

The mesh quality report has been generated by the 'checkMesh' command in openFoam.

Mesh Parameter	Value
Max aspect ratio	18.7872
Max non-orthogonality	50.8869 Average: 14.1406
Max skewness	1.63729
Max cell openness	$5.15435 \times 10^{-16}$

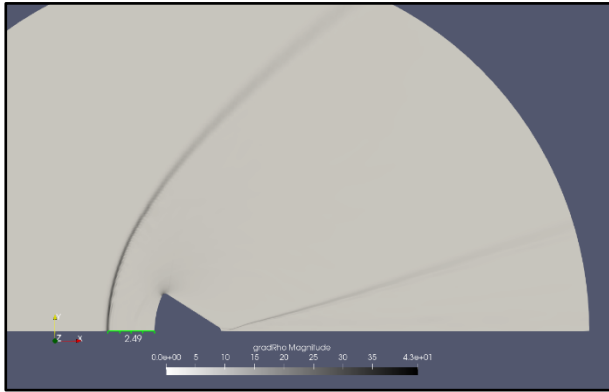
Table 13: Mesh Quality Table

## 5.3 Results

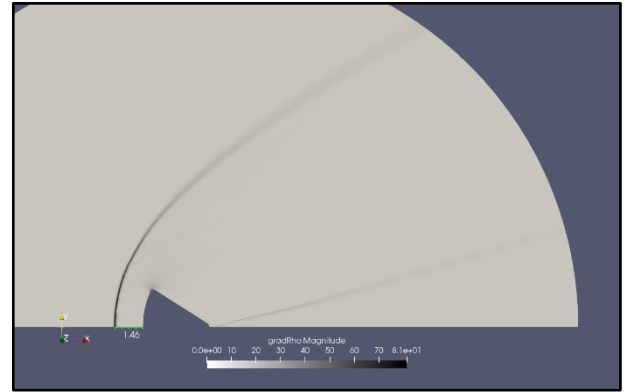
### 5.3.1 Schlieren Graphs and Shock distances

The density gradients for the re-entry bodies can be observed below.

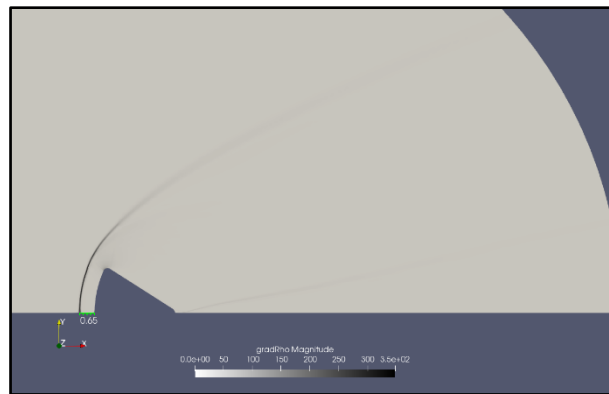
#### A. Apollo



(a) Mach 2.7



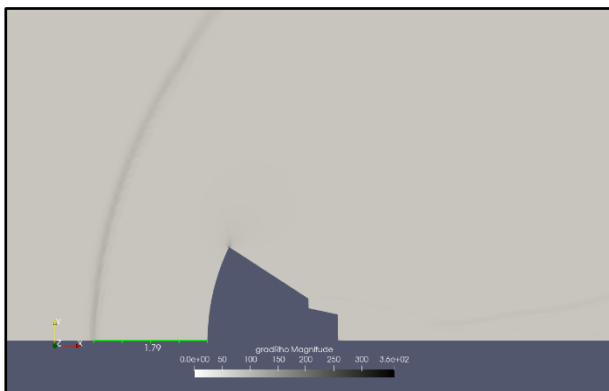
(b) Mach 4



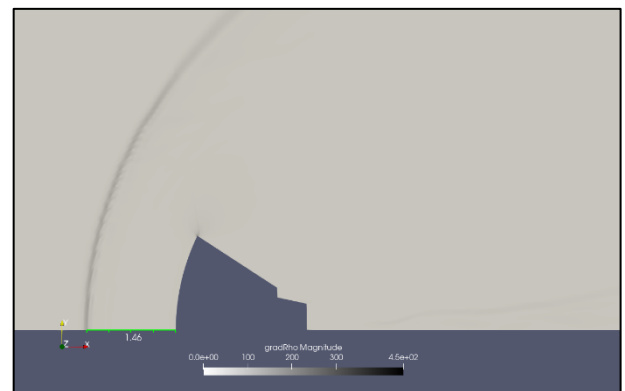
(c) Mach 6

Figure 5.5 Schlieren Graph for Apollo

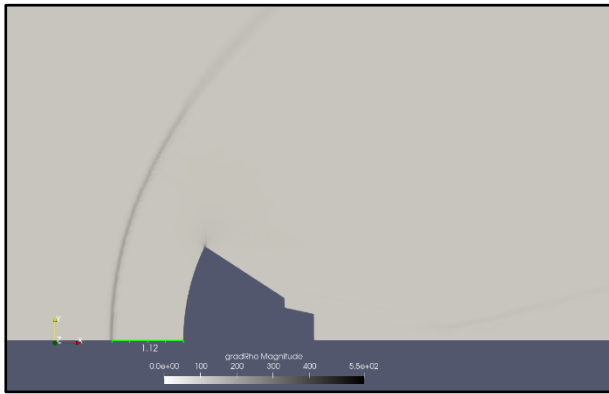
#### B. ARD



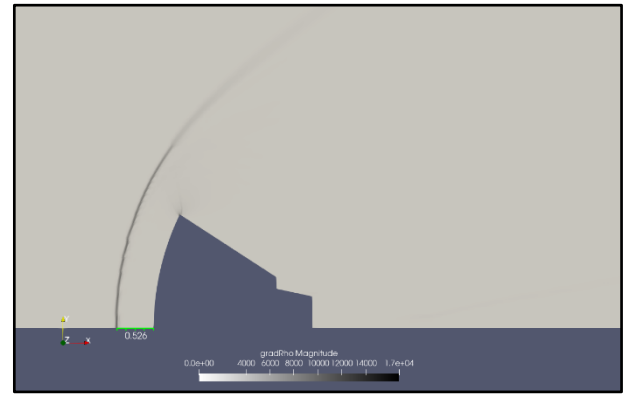
(a) Mach 2.7



(b) Mach 3.35



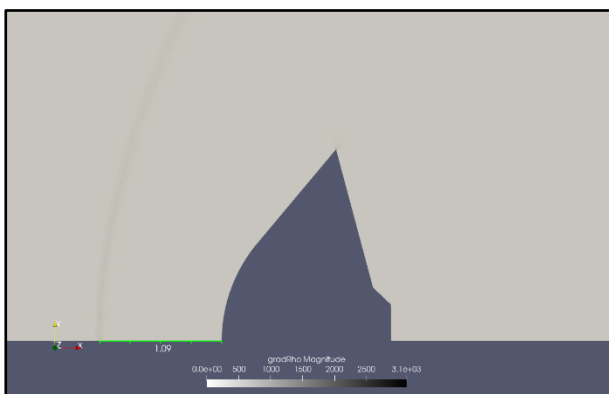
(c) Mach 4



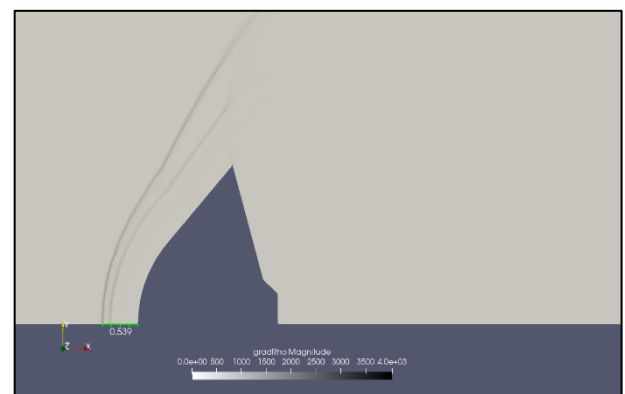
(d) Mach 6

Figure 5.6 Schlieren Graph for ARD

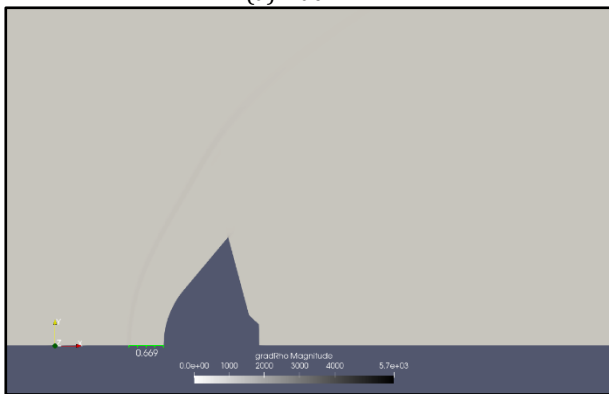
## C. OREX



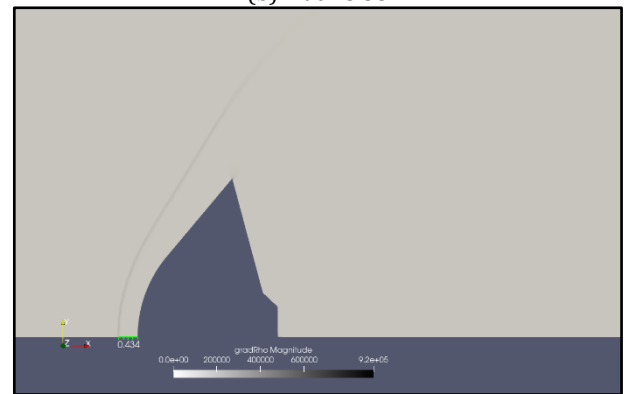
(a) Mach 2.7



(b) Mach 3.35



(c) Mach 4



(d) Mach 6

Figure 5.7 Schlieren Graph for OREX

Here, for OREX  $M=3.35$  we can observe some inaccuracies and errors observed due to the formation of double shocks. This can be even observed in the shock distance of the first shock been closer to the body as compared to the shock of  $M=4$ .



## D. Shock stand-off distances

Shock distances for each body at various  $M_1$  can be observed in the table below

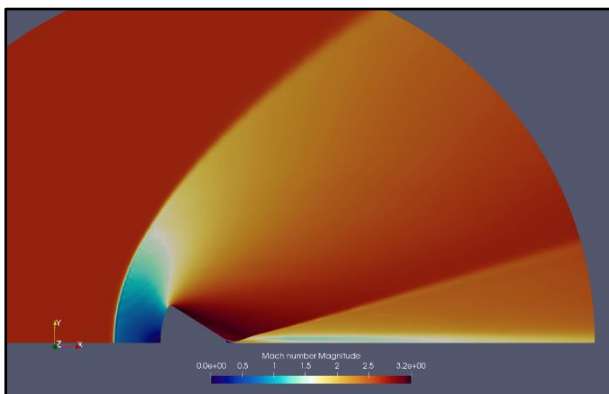
Body	Mach number	Shock Stand-off Distance (d)
Apollo	2.7	2.49 m
	4.0	1.46 m
	6.0	0.65 m
ARD	2.7	1.79 m
	3.35	1.46 m
	4.0	1.12 m
	6.0	0.526 m
OREX	2.7	1.09 m
	3.35	1.539 m
	4.0	0.669 m
	6.0	0.434 m

Table 14: Shock distances for all bodies

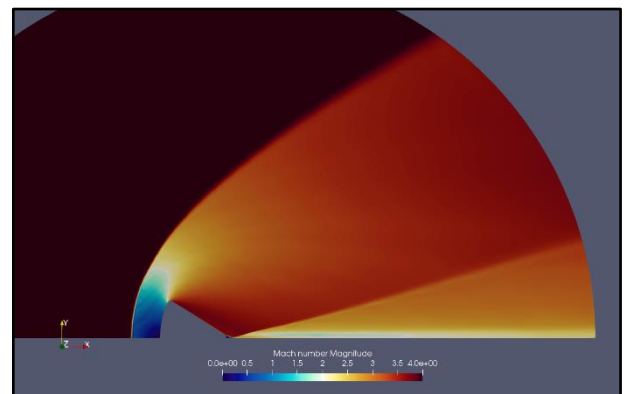
### 5.3.2 Velocity over the body

To observe the velocity profile over the cylinder, we use Mach number contours. As expected from the contours, we can see as the velocity increases, the intensity and strength of the shock waves generally increase as well. We can also observe that the increase in velocity also brings the shock closer to the body.

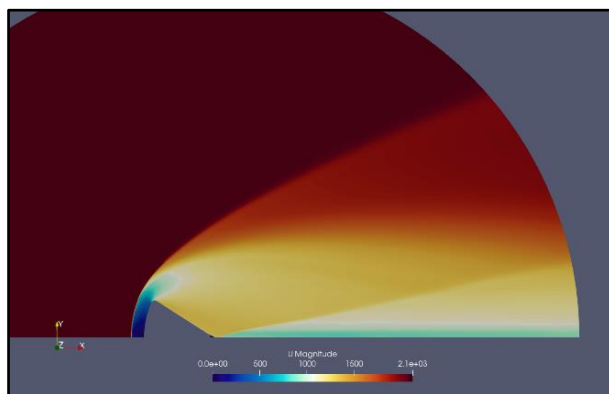
#### A. Apollo



(a) Mach 2.7



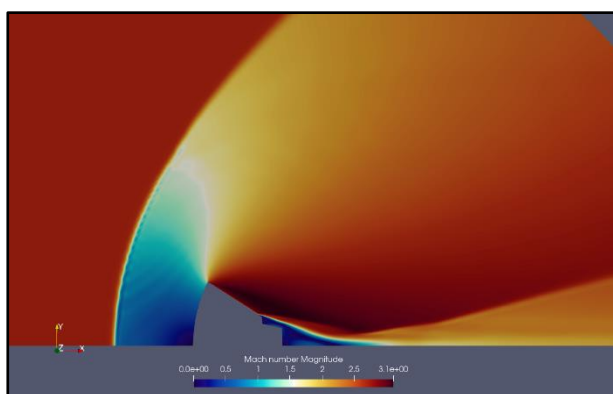
(b) Mach 4



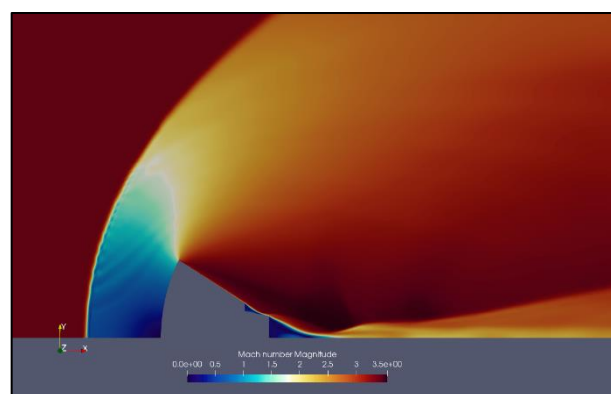
(c) Mach 6

Figure 5.8 Mach Contours for Apollo

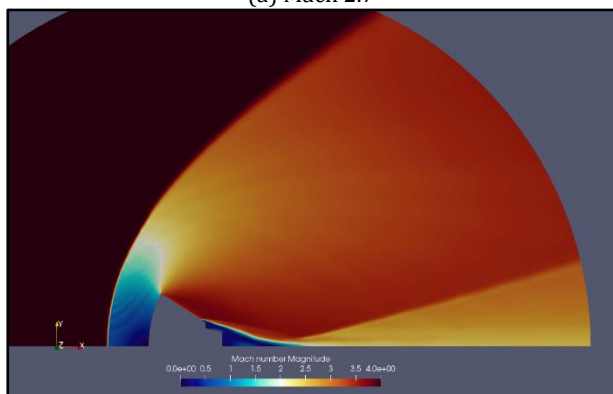
## B. ARD



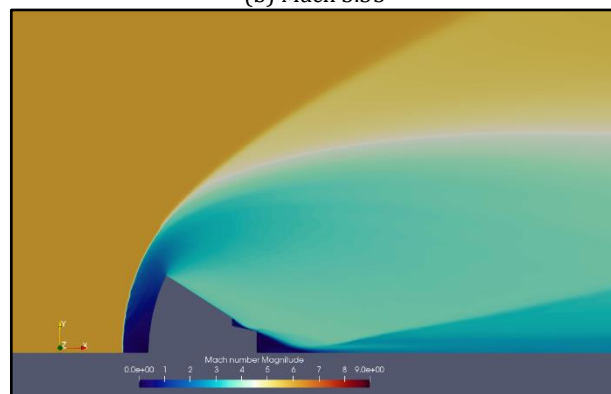
(a) Mach 2.7



(b) Mach 3.35



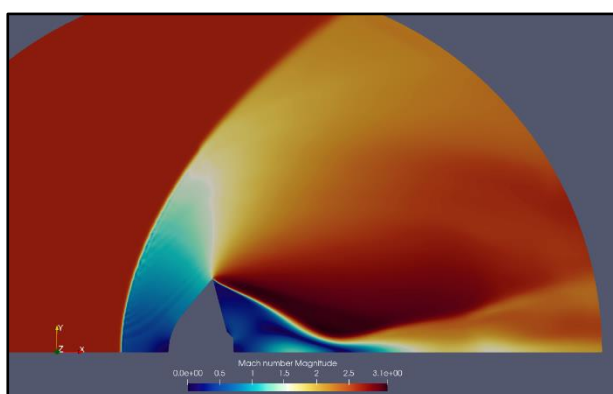
(c) Mach 4



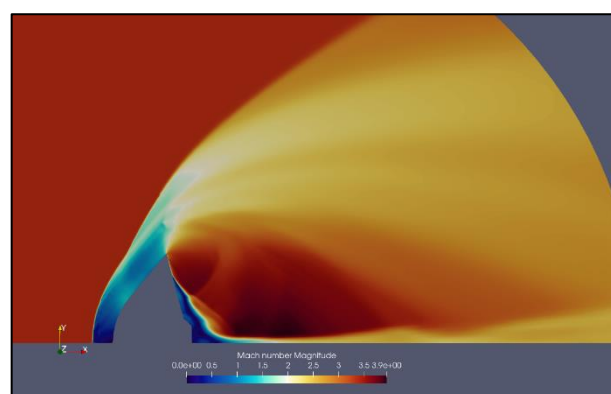
(d) Mach 6

Figure 5.9 Mach Contours for ARD

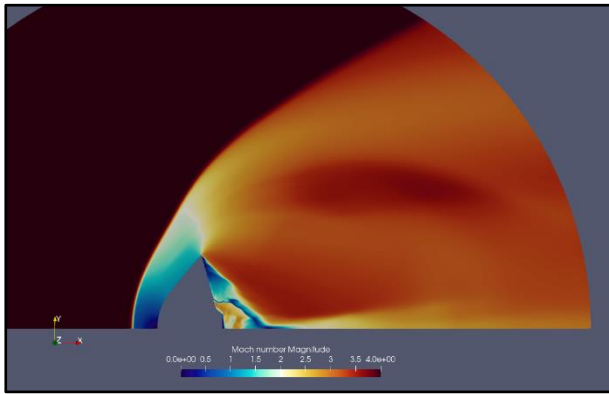
## C. OREX



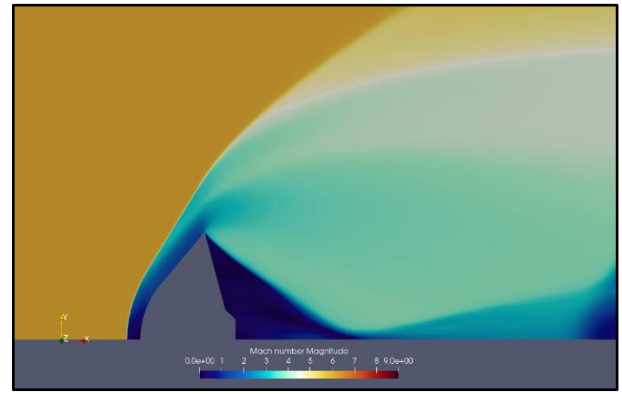
(a) Mach 2.7



(b) Mach 3.35



(c) Mach 4



(d) Mach 6

Figure 5.10 Mach Contours for OREX

### 5.3.1 Pressure Distribution

The pressure distribution plays a major role in depicting the drag and behavior of the body in supersonic/hypersonic flow. Here are the pressure distribution plots for the re-entry bodies described using pressure coefficients ( $C_p$ ) vs the X-co-ordinates along the body surface. The bodies are also shown faintly to describe the areas with pressure drops and rises along with their respective stagnation pressure values.

From the plots, we can tell similarly about the inaccuracy of OREX at  $M=3.35$ .

#### A. Apollo

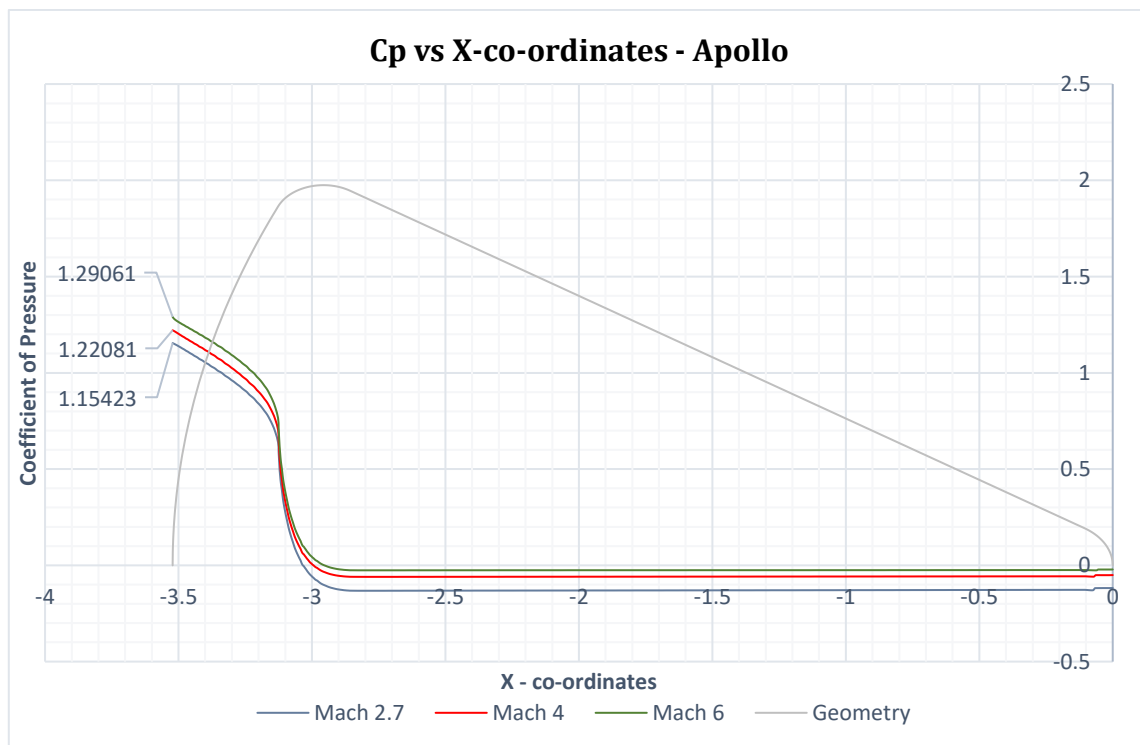


Figure 5.11 Pressure Distribution for the Apollo Capsule



## B. ARD

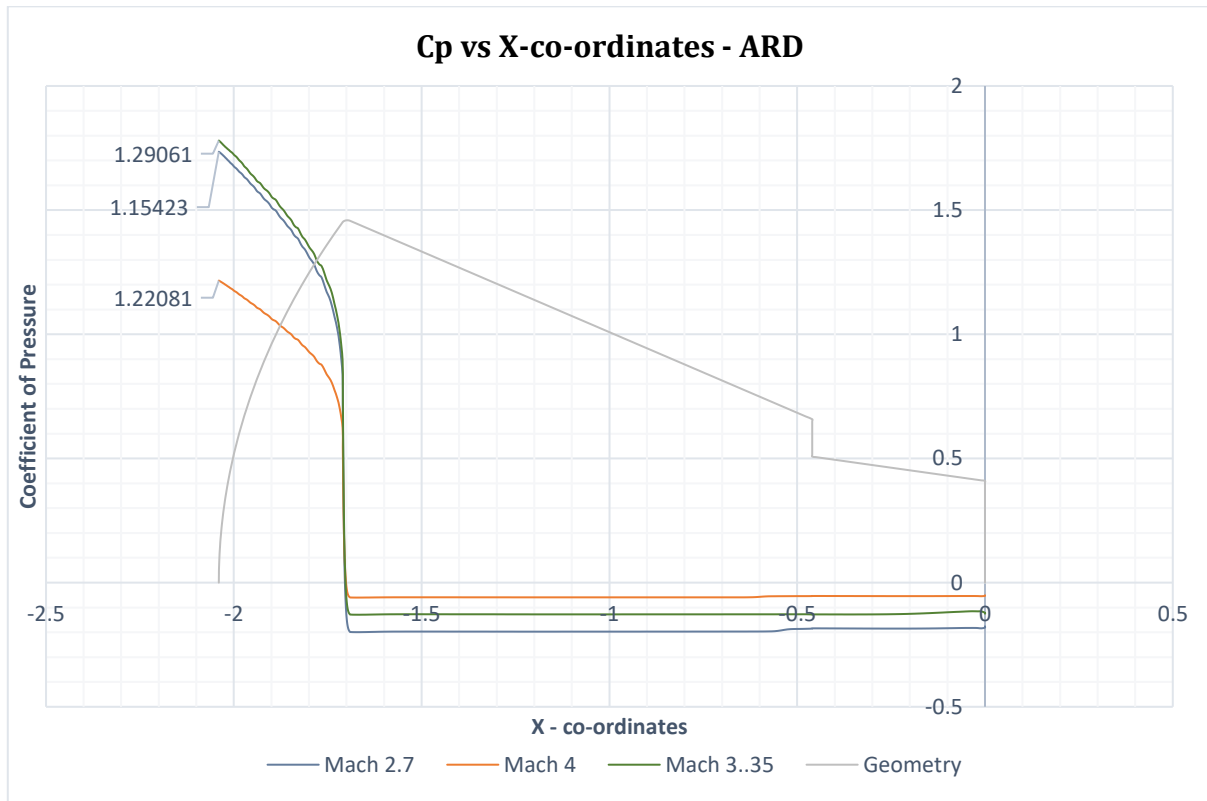


Figure 5.12 Pressure Distribution for the ARD Capsule

## C. OREX

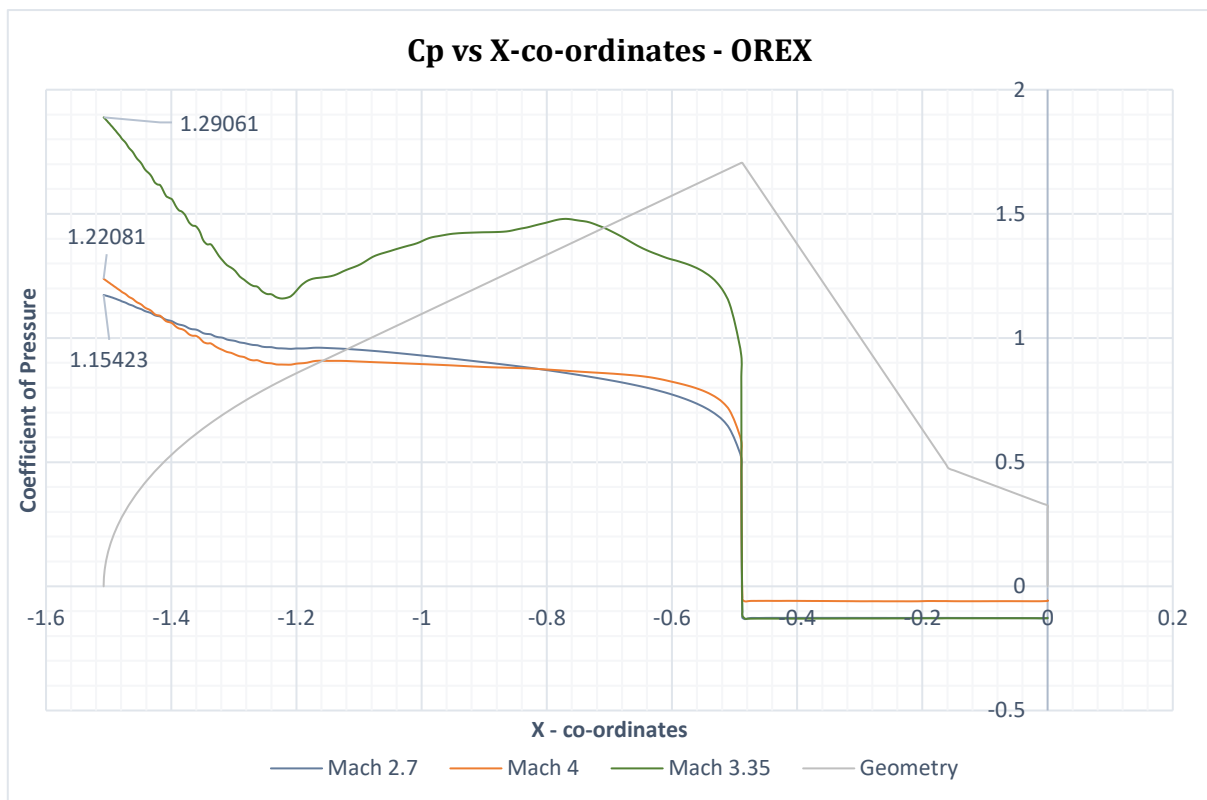
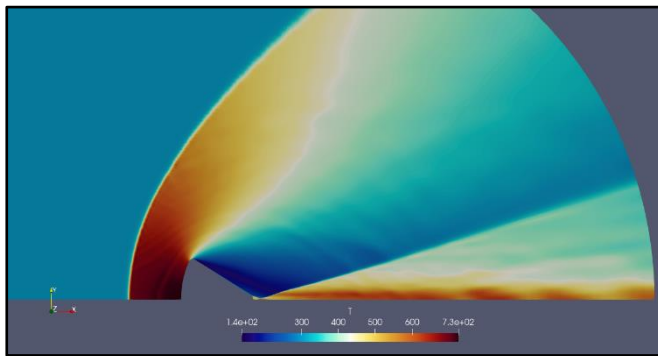


Figure 5.13 Pressure Distribution for the OREX Capsule

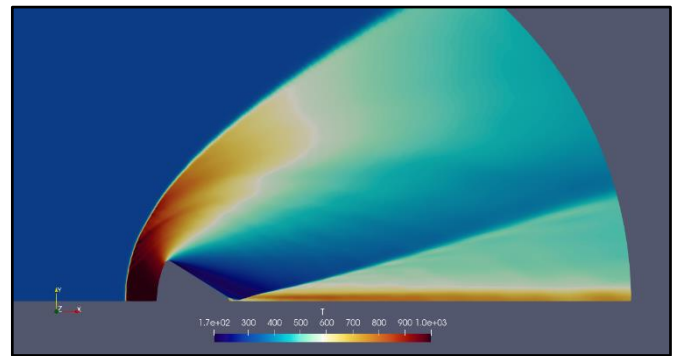
### 5.3.2 Temperature Contours

The temperature contours can tell about the heat dissipation and can be further used in future work to depict heat transfer due to aerodynamic heating. At  $M_1 = 6$ , we can observe the dissipation more clearly as aerodynamic heating is more dominant at hypersonic speeds.

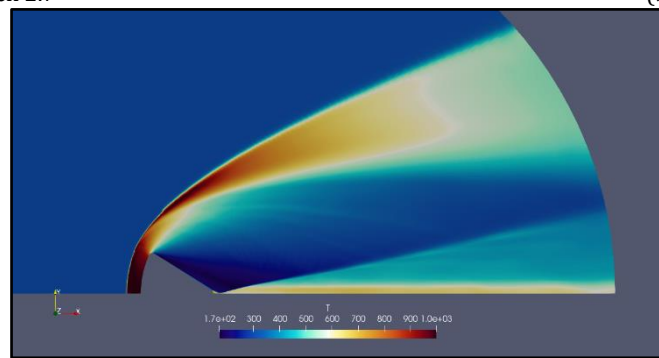
#### A. Apollo



(a) Mach 2.7



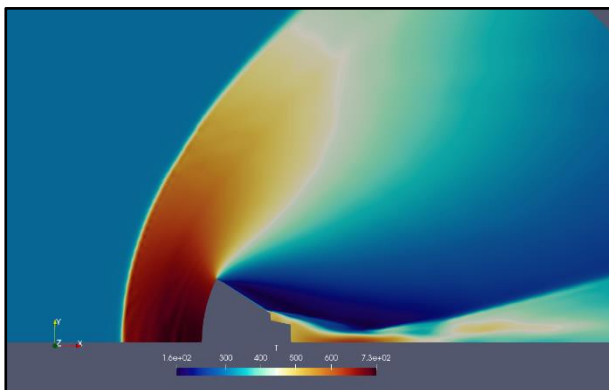
(b) Mach 4



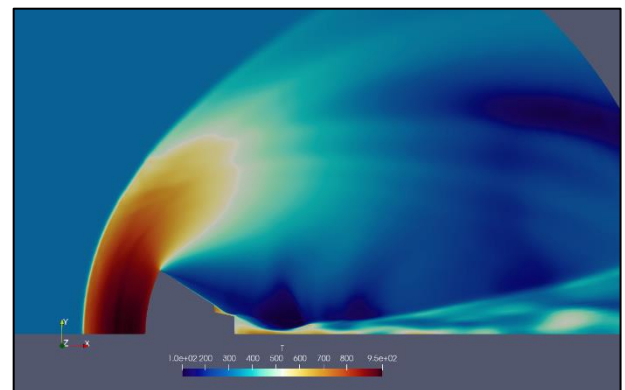
(c) Mach 6

Figure 5.14 Temperature Contours for Apollo

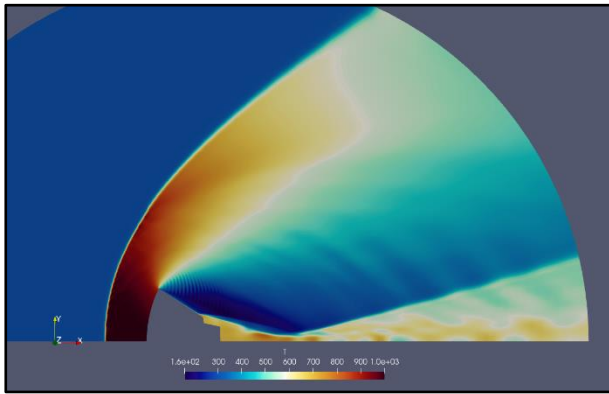
#### B. ARD



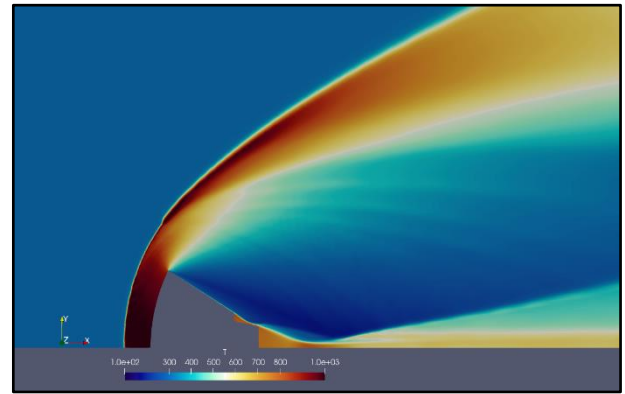
(a) Mach 2.7



(b) Mach 3.35



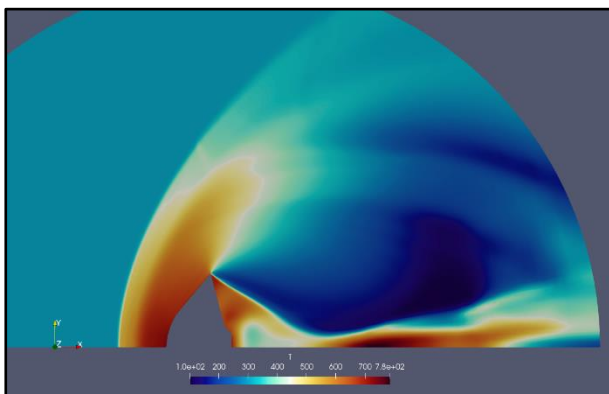
(c) Mach 4



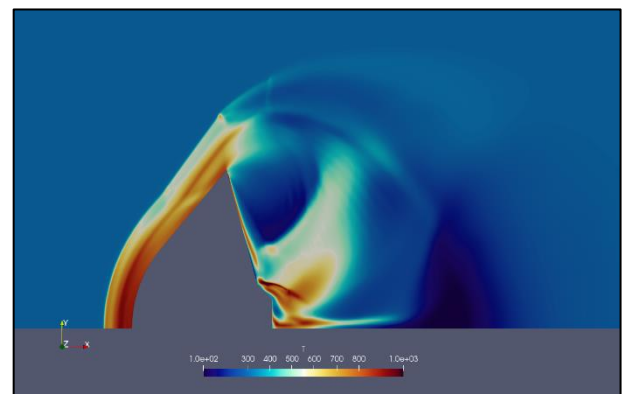
(d) Mach 6

Figure 5.15 Temperature Contours for ARD

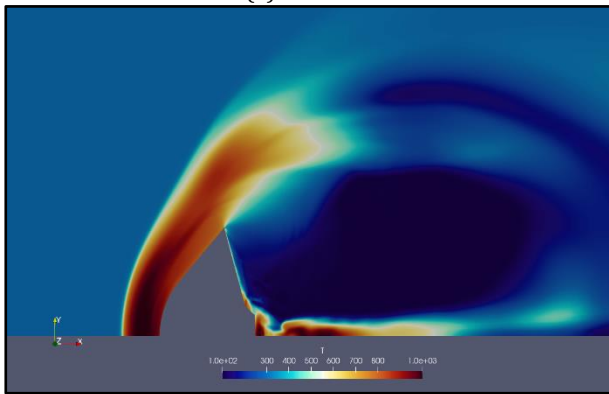
### C. OREX



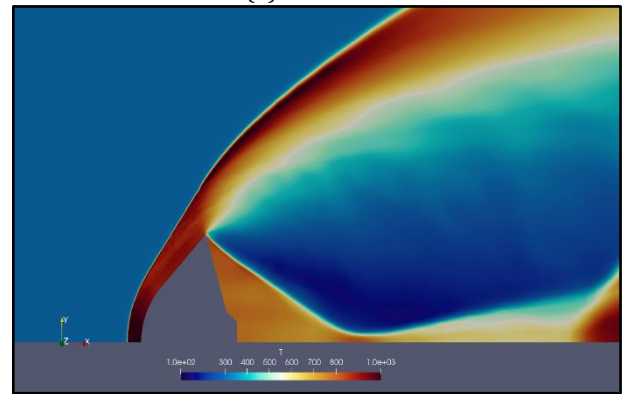
(a) Mach 2.7



(b) Mach 3.35



(c) Mach 4



(d) Mach 6

Figure 5.16 Temperature Contours for Apollo

From, the temperature contours, we can also see about the inaccuracies at flow of  $M=3.35$ .

### 5.3.3 Drag Estimation

A re-entry body always needs to be optimized for high drag and high thermal insulation so during the re-entry the body slows down and does not burn up in the atmosphere due to the aerodynamic heating. For the drag, the simulation results are shown in the table below for the re-entry bodies.

From, the values itself, we can observe errors and inaccuracies while in the calculation of the drag for OREX and ARD bodies at  $M=6$ .

Body	Mach number	Drag Force (N)	Drag Coefficient ( $C_D$ )
Apollo	2.7	14,68,796	0.732
	4.0	31,92,766	0.725
	6.0	73,89,490	0.745
ARD	2.7	5,81,001	0.618
	3.35	884182	0.611
	4.0	12,61,737	0.611
	6.0	3,73,21,600	8.038
OREX	2.7	5,43,246	0.710
	3.35	814168	0.691
	4.0	11,21,870	0.668
	6.0	19,68,46,000	52.070

Table 15: Drag values for all bodies

# Chapter 5

## Conclusion

### 5.1 Conclusion

A numerical study was conducted to validate and investigate high-speed compressible turbulent flow over a blunt body. A validation was performed for the experimental results of Kim, Chul Soo [1] by comparing various plots for the given Mach number flows. The study was further extended by implementing various re-entry capsules which was used by R.C. Mehta [2] [4] [5] in the flow and studying the effect of various Mach numbers which affects the Pressure distribution, Velocity profiles and Aerodynamic forces. In addition, a small study for the temperature dissipation was shown which can be used to further extend this study for investigating heat transfers at hypersonic flow regimes even with the possibility to study the ionization of the air and study the chemical non-equilibrium flows over such bodies. We have also managed to conclude that 'sonicFoam', a pressure based compressible openFoam solver lacks accuracy in the hypersonic regime wherein the solver couldn't compute the pressure distributions and shock structures with accurate results. A mesh independence study was also conducted and the least computationally expensive, yet accurate mesh size was determined.

## References

1. Kim<sup>1</sup>, Chul-Soo<sup>2</sup> " Experimental Studies of Supersonic Flow past a Circular Cylinder". In: *Journal of the Physical Society of Japan Vol. 11, No. 4, 1956*
2. R.C.Mehta<sup>1</sup> "Numerical Computation of Heat Transfer on Reentry Capsules at Mach 5". In: *43rd AIAA Aerospace Sciences Meeting and Exhibit, 2005*
3. Mehta, R. (2019). "Numerical Simulation of Base Pressure and Drag of Space Reentry Capsules at High Speed" In: *Hypersonic Vehicles-Past, Present and Future Developments, 2019.*
4. R.C.Mehta<sup>1</sup> "Numerical Computation of Heat Transfer on Reentry Capsules at Mach 5". In: *43rd AIAA Aerospace Sciences Meeting and Exhibit, 2005*". In: *Indian Journal of Engineering and Material , 2008*
5. <https://openfoamwiki.net/index.php/sonicFoam>
6. Dirkx, Dominic & Mooij, Erwin. (2011). "Continuous Aerodynamic Modelling of Entry Shapes". In: *AIAA Atmospheric Flight Mechanics Conference 2011.*
7. Shiva Prasad U.<sup>1</sup>, Srinivas G.<sup>2</sup>. "Flow Simulation over Re-Entry Bodies at Supersonic & Hypersonic Speeds" In: *International Journal of Engineering Research and Development, 2012.*
8. John D Anderson Jr<sup>1</sup>. "COMPUTATIONAL FLUID DYNAMICS: The Basics with Applications." Department of Aerospace Engineering, University of Maryland, 1995.
9. James N. Moss\*, Christopher E. Glass<sup>1</sup> and Francis A. Greenez<sup>2</sup>. "DSMC Simulations of Apollo Capsule Aerodynamics for Hypersonic Rareed Conditions". In: *7th AIAAASM Thermophysics and Heat Transfer Conference. 2005.*
10. Luther Neal, Jr.. "Life at low Reynolds number." *American Journal of Physics, 1977.*
11. Pratik Das<sup>1</sup>, Ashoke De<sup>2</sup>. "Numerical investigation of flow structures around a cylindrical afterbody under supersonic condition". In: *Aerospace Science and Technology. Volume 47, 2015.*
12. Oded Regev<sup>1</sup>, Orkan M. Umurhan<sup>2</sup> & Philip A. Yecko<sup>3</sup>. "Chapter: Effects of Compressibility, Modern Fluid Dynamics for Physics and Astrophysics", 2016.
13. Ivey, Christopher & Danehy, Paul & Bathel, Brett & Dyakonov, Artem & Inman, Jennifer & Jones, Stephen. (2011). "Comparison of PLIF and CFD Results for the Orion CEV RCS Jets". In: *49th AIAA Aerospace Sciences Meeting including the New Horizons Forum and Aerospace Exposition. 2011.*